The Astrophysical Journal, 662:443–458, 2007 June 10


# *SWIFT* AND *XMM-NEWTON* OBSERVATIONS OF THE EXTRAORDINARY GAMMA-RAY BURST 060729: MORE THAN 125 DAYS OF X-RAY AFTERGLOW

Dirk Grupe,[1] Caryl Gronwall,[1] Xiang-Yu Wang,[1,2] Peter W. A. Roming,[1] Jay Cummings,[3] Bing Zhang,[4] Peter Mészáros,[1,5] Maria Diaz Trigo,[6] Paul T. O'Brien,[7] Kim L. Page,[7] Andy Beardmore,[7] Olivier Godet,[7] Daniel E. vanden Berk,[1] Peter J. Brown,[1] Scott Koch,[1] David Morris,[1] Michael Stroh,[1] David N. Burrows,[1] John A. Nousek,[1] Margaret McMath Chester,[1] Stefan Immler,[8,9] Vanessa Mangano,[10] Patrizia Romano,[11] Guido Chincarini,[11] Julian Osborne,[7] Takanori Sakamoto,[3] and Neil Gehrels[3]

*Received 2006 November 7; accepted 2007 February 28*

## ABSTRACT

We report the results of the *Swift* and *XMM-Newton* observations of the *Swift* -discovered GRB 060729 ($T_{90} = 115$ s). The afterglow of this burst was exceptionally bright in X-rays as well as at UV/optical wavelengths, showing an unusually long slow decay phase ($\alpha = 0.14 \pm 0.02$), suggesting a larger energy injection phase at early times than in other bursts. The X-ray light curve displays a break at about 60 ks after the burst. The X-ray decay slope after the break is $\alpha = 1.29 \pm 0.03$. Up to 125 days after the burst we do not detect a jet break, suggesting that the jet opening angle is larger than 28°. We find that the X-ray spectra of the early phase change dramatically and can all be fitted by an absorbed single–power-law models or alternatively by a blackbody plus power-law model. The power-law fits show that the X-ray spectrum becomes steeper while the absorption column density decreases. In the blackbody model the temperature decreases from $kT = 0.6$ to 0.1 keV between 85 and 160 s after the burst in the rest frame. The afterglow was clearly detected up to 9 days after the burst in all six UVOT filters and in UVW1 even for 31 days. A break at about 50 ks is clearly detected in all six UVOT filters from a shallow decay slope of about 0.3 and a steeper decay slope of 1.3.The *XMM-Newton* observations started about 12 hr after the burst and show a typical afterglow X-ray spectrum with $\beta_X = 1.1$ and absorption column density of $1 \times 10^{21}$ cm$^{-2}$.

*Subject headings:* gamma rays: bursts — X-rays: bursts

*Online material:* color figure

## 1. INTRODUCTION

Gamma-ray bursts (GRBs) are the most powerful explosions in the present-day universe. With the launch of the *Swift* Gamma-Ray Burst Explorer Mission (Gehrels et al. 2004) in 2004 November a new era in GRB science has started. *Swift* is able to observe the afterglow of a burst with its narrow-field instruments, the X-Ray Telescope (XRT; Burrows et al. 2005a) and the UV/Optical telescope (UVOT; Roming et al. 2005), typically within 2 minutes after the detection by the Burst Alert Telescope (BAT; Barthelmy et al. 2005). Several phenomena were discovered by *Swift*, such as the occurrence of giant flares during the first 1000 s after the burst (e.g., Burrows et al. 2005b; Falcone et al. 2006) or the canonical light curves of GRB afterglows (Nousek et al. 2006; Zhang et al. 2006).

GRB 060729 was discovered by *Swift* on 2006 July 29 (Grupe et al. 2006) as one of the brightest bursts ever detected by the device in X-rays (with the brightest GRB observed by XRT so far being GRB 061121; Page et al. 2007). Besides GRB 050525A (Blustin et al. 2006), GRB 060218 (Campana et al. 2006), GRB 060614 (Mangano et al. 2007), and GRB 061121 (Page et al. 2007), GRB 060729 is the burst with the best UVOT follow-up even up to 9 days after the burst in all six UVOT filters and even longer in some of the UV filters. XRT has detected the afterglow more than 125 days after the burst. This is the longest follow-up observation with a detection of an afterglow ever performed by *Swift*. Similar, but shorter, coverage has only been performed for GRB 050416A, GRB 060319, and GRB 060614. Even though the burst was bright in the BAT, it was too faint to be detected by Konus-*Wind* (D. D. Frederiks 2006, private communication).

Even though the Sun angle was small in right ascension (2.2 hr), due to the declination −62°, the afterglow was circumpolar for most southern observatories and was observed by the ESO Very Large Telescope (VLT) using FORS2 and by Gemini South using GMOS (Thoene et al. 2006). A redshift of $z = 0.54$ was determined from the optical spectra by Thoene et al. (2006). GRB 060729 was also observed by ROTSE IIIa, located at the Siding Spring Observatory, Australia, by Quimby et al. (2006), who reported an initial upper limit of 16.6 mag 64 s after the BAT trigger. They were able to detect the afterglow with ROTSE IIIa up to 175 ks after the burst when it was still at 19.4 mag (Quimby & Rykoff 2006), decaying with a slope $\alpha = 0.23$. Cobb & Bailyn (2006) measured a decay slope in the $I$ band of $\alpha_I = 1.5$ based on CTIO 1.3 m SMARTS observations between 4.6 to 17.6 days after the burst.

[1] Department of Astronomy and Astrophysics, Pennsylvania State University, University Park, PA 16802; grupe@astro.psu.edu.
[2] Department of Astronomy, Nanjing University, Nanjing 210093, China.
[3] Astrophysics Science Division, Astroparticle Physics Laboratory, NASA Goddard Space Flight Center, Greenbelt, MD 20771.
[4] Department of Physics, University of Nevada, Las Vegas, NV 89154.
[5] Department of Physics, Pennsylvania State University, University Park, PA 16802.
[6] *XMM-Newton* Science Operations Centre, European Space Agency, Villafranca del Castillo, 28080 Madrid, Spain.
[7] Department of Physics and Astronomy, University of Leicester, Leicester LE1 7RH, UK.
[8] Astrophysics Science Division, X-Ray Astrophysical Laboratory, NASA Goddard Space Flight Center, Greenbelt, MD 20771.
[9] Universities Space Research Association, Columbia, MD 21044.
[10] INAF–Istituto di Astrofisica Spaziale e Fisica Cosmica di Palermo, I-90146 Palermo, Italy.
[11] INAF–Osservatorio Astronomico di Brera, I-23807 Merate, Italy.

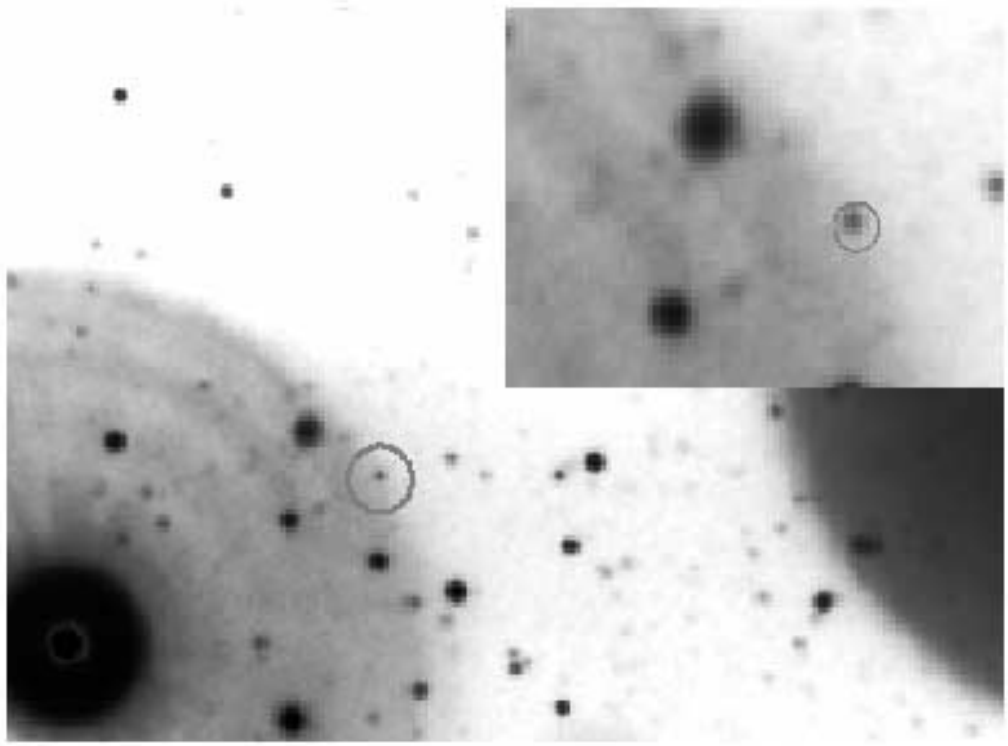

FIG. 1.—UVW1 image ($5.7' \times 4.2'$) of the field of GRB 060729 with an exposure of 550 ks. The circles at the source position displays the XRT position as given in § 3.1. The circles in the large image show a $8''$ radius at the source just for display purposes, and the $8''$ background extraction region. The zoom-in image ($80'' \times 60''$) in the top right corner shows the $3.5''$ XRT error radius. Note the bright star that is only $107''$ away from the position of the afterglow of GRB 060729. [*See the electronic edition of the Journal for a color version of this figure*.]

The paper is organized as follows. In § 2 we describe the observations and the data reduction. In § 3 we present the data analysis. The discussion of our results is given in § 4. Throughout the paper decay and energy spectral indices $\alpha$ and $\beta$ are defined by $F_\nu(t,\ \nu) \propto (t - t_0)^{-\alpha} \nu^{-\beta}$, with $t_0$ the trigger time of the burst. Luminosities are calculated assuming a $\Lambda$CDM cosmology with $\Omega_M = 0.27$, $\Omega_\Lambda = 0.73$, and a Hubble constant of $H_0 = 71$ km s$^{-1}$ Mpc$^{-1}$ using the luminosity distances $D_L$ given by Hogg (1999), resulting in $D_L = 3120$ Mpc. All errors are 1 $\sigma$ unless stated otherwise.

## 2. OBSERVATIONS AND DATA REDUCTION

The *Swift* BAT triggered on the precursor of GRB 060729 at 19:12:29 UT on 2006 July 29 (Grupe et al. 2006; Grupe 2006). *Swift*'s XRT began observing the afterglow 124 s after the trigger. The UVOT started the observations 135 s after the BAT trigger.

The *Swift* XRT observed GRB 060729 in the windowed timing (WT) and photon counting (PC) observing modes (Hill et al. 2004). The XRT data were reduced by the `xrtpipeline` task version 0.10.4. The WT mode data at the beginning of the XRT observation had to be treated with special care. During the first 20 s after the start (130–150 s after the BAT trigger) of the WT XRT observation the satellite was still settling, causing the target to move on the XRT CCD toward the dead columns at DETX = 319–321 (Abbey 2006). In order to correct for the photon losses due to these dead columns we measured the offset of the source at each second and calculated a correction factor according to the losses of the WT mode point-spread function (PSF). After 150 s after the trigger all WT mode data were corrected by the same factor. Source and background photons were selected by XSELECT version 2.4 in boxes with a length of 40 pixels. For count rates >150 counts s$^{-1}$, however, in the WT mode the data had to be corrected for pileup. In order to correct for pileup in the light curve and for the spectral analysis and the determination of the hardness ratio[12] we excluded the central regions of the PSF at the source position, depending on the count rate as described in Romano et al. (2006). For the PC mode data the source photons were selected in a circular region with a radius of $r = 59''$ and the background photons in a circular region close by with a radius $r = 176''$ in the first segments. For the later data the radii were reduced to $47''$ and $24''$ for the source and $137''$ and $96''$ for the background. For the spectral data only events with grades 0–2 and 0–12 were selected with XSELECT for the WT and PC mode data, respectively. Note that the source photons for the spectral analysis of the PC mode data of the first orbit were selected in a ring with an inner radius of $16.5''$ and an outer radius of $71.0''$ in order to avoid the effects of pile-up (e.g., Pagani et al. 2006; Vaughan et al. 2006). The spectral data were rebinned by using `grppha` version 3.0.0, with 20 photons bin$^{-1}$. The spectra were analyzed with XSPEC version 12.3.0 (Arnaud 1996). The auxiliary response files were created by `xrtmkarf` and corrected using the exposure maps, and the standard response matrices `swxwt0to2_20010101v008.rmf` and `swxpc0to12_20010101v008.rmf` were used for the WT and PC mode data, respectively. All spectral fits were performed in the observed 0.3–10.0 keV energy band. For the errors of the spectral fit parameters we used the standard $\Delta\chi^2 = 2.7$ in XSPEC, which is equivalent to a 90% confidence region for a single parameter.

Background-subtracted X-ray flux light curves in the 0.3–10.0 keV energy range of the *Swift* observations were constructed

[12] The hardness ratio is defined by HR = (hard − soft)/(hard + soft) where "soft" is the counts in the 0.3-1.0 keV band and "hard" is the counts in the 1.0–10.0 keV band, respectively.

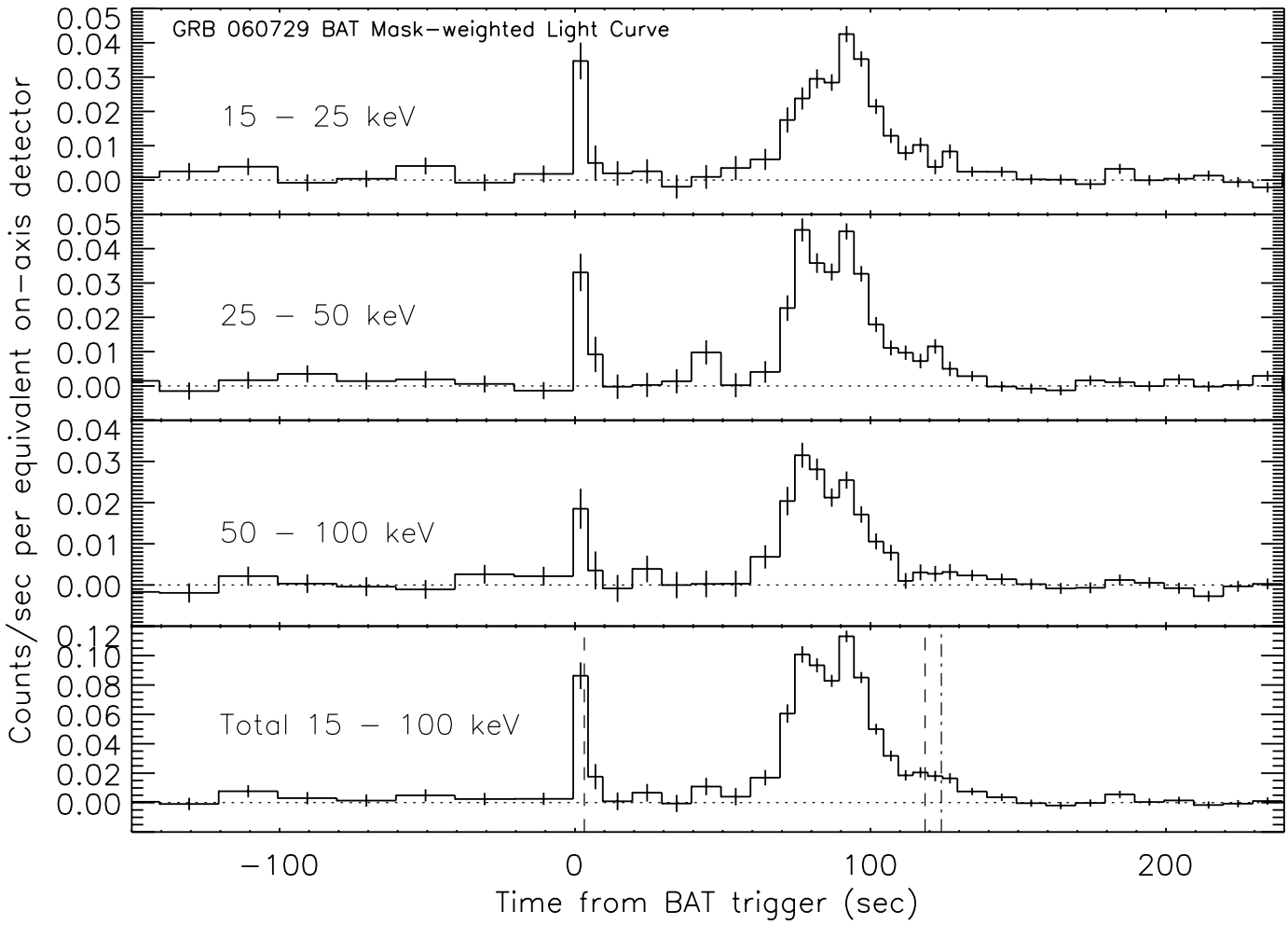


FIG. 2.—*Swift* BAT light curves in the (*top to bottom*) 15–25, 25–50, 50–100, and 15–100 keV band. The vertical dashed line in the 15–100 keV plot marks the time for which $T_{90}$ was calculated and the dotted-dashed line the beginning of the XRT observations at 124 s after the burst.

using the ESO Munich Image Data Analysis Software (MIDAS vers. 04Sep) and by an IDL program that corrects for PSF losses, in particular when the source is located on one of the dead columns on the XRT CCD detector. The light curve was binned as follows: the WT mode data with 1000 photons bin$^{-1}$, and the pc mode data with 200 counts bin$^{-1}$ in the first days after the burst and 20 or 10 at the end of the observations. The count rates were converted into unabsorbed flux units using energy conversion factors (ECF) that were determined by calculating the count rates and the unabsorbed fluxes in the 0.3–10.0 keV energy band using XSPEC as described in Nousek et al. (2006). The XRT data at the beginning of the observation show dramatic spectral changes and require specific ECFs for each time bin. The later data, however, do agree with a typical afterglow spectrum, and the count rates were converted by one ECF $= 5 \times 10^{-11}$ ergs s$^{-1}$ cm$^{-2}$ (counts s$^{-1}$)$^{-1}$.

The *Swift* UVOT observations of GRB060729 began with the automated GRB sequence, which provided finding chart images in white (100 s) and $V$ (400 s), and then began cycling through all six UV and optical filters starting 739 s after the trigger. The source data of these early white and $V$ images were extracted from a circle with a radius of 6″. GRB 060729 remained detectable in all six filters for more than 9 days after the trigger, then for 12 days after the trigger in UVW2 ($\lambda_c = 1930$ Å) and for 31 days after the trigger in UVW1 ($\lambda_c = 2510$ Å). During the first days after the burst each observation in each single orbit was analyzed. For the later data the images were co-added with `uvotimsum` in order to improve the signal-to-noise ratio (S/N). The data were analyzed with the UVOT software tool `uvotsource`. Due to the bright F3 V star HD 45187 (9.4 mag in $B$, 107.5″ away from GRB 060729) extra caution had to be taken for the source extraction and the background subtraction. We chose a selection radius of 4″ for the source and 8″ for the background in all filters placed at a position nearby on the rim of the bright star's halo, as displayed in Figure 1. In order to correct for losses due to this small source extraction radius, we did an aperture correction with $V = 0.03$, $B = 0.05$, $U = 0.05$, UVW1 $= 0.17$, UVM2($\lambda_c = 2170$ Å) $= 0.15$, and UVW2 $= 0.15$ mag. All values plotted and listed in this paper take these corrections into account. The data, however, are not corrected for Galactic reddening, which is $E_{B-V} = 0.050$ mag (Schlegel et al. 1998) in the direction of the burst.

GRB 060729 was also observed by *XMM-Newton* (Jansen et al. 2001) for a total of 61 ks (Schartel 2006; Campana & De Luca 2006). *XMM-Newton* started observing the afterglow of GRB 060729 on 2006 July 30 07:41 (44.9 ks after the trigger) and continued observations until 2006 July 31 01:04 UT (107.5 ks after the trigger). In the European Photon Imaging Camera (EPIC) pn (Strüder et al. 2001) the total observing time was 59.6 ks using the medium light blocking filter. However, due to high particle background during part of the observation only 42.3 ks were used. The observations in the EPIC MOS (Turner et al. 2001) were for a total observing time of 61.2 ks. The MOS1 was using the medium filter, while the MOS2 observations were performed with the thin filter. The total observing time in the reflection grating spectrometers (RGSs; den Herder et al. 2001) was 61.5 ks. In

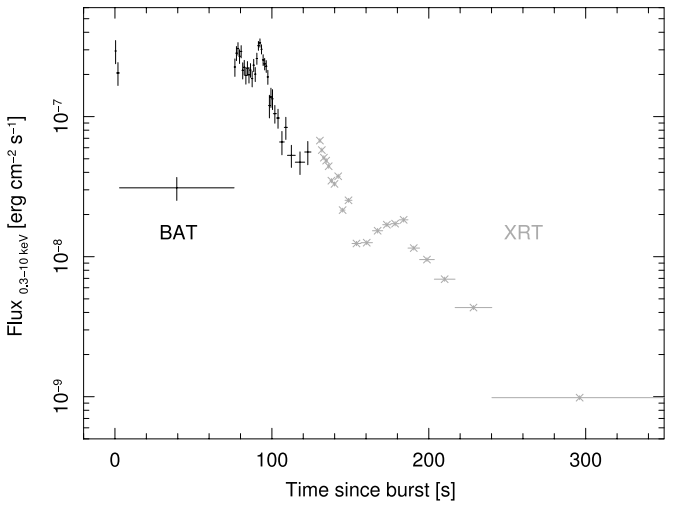


FIG. 3.—Combined *Swift* BAT and XRT WT light curves. The figure clearly shows that the XRT was starting observing GRB 060729 during the fourth peak seen in the BAT.

the optical monitor (OM; Mason et al. 2001) the afterglow was observed for 8.3 ks in $U$, $5 \times 4$ ks in UVW1, $3 \times 4$ ks in UVM2, and $2 \times 4$ ks with the optical grism. Note that the OM UVW1 and UVM2 filters are slightly different compared with the UVOT UV filters. The *XMM-Newton* data were reduced with the latest SAS version `xmmsas_20060628_1801-7.0.0`.

## 3. DATA ANALYSIS

### 3.1. *Position of the Afterglow*

The position of the afterglow measured from the UVOT UVW1 co-added image is R.A. (J2000.0) = $06^h21^m31.86^s$, decl. (J2000.0) = $-62^\circ22'12.5''$ with a $1''$ error. This position is consistent with the initial analysis of the white and $V$ filter analysis (Immler 2006). The UVW1 position is $1.1''$ away from the X-ray position R.A. (J2000.0) = $06^h21^m31.75^s$, decl. (J2000.0) = $-62^\circ22'13.3''$ (with a $3.5''$ 90% confidence error), which was measured for the XRT PC mode data of segment 001 using the new `teldef` file `swx20060402v001.teldef` as described in Burrows et al. (2006). This position deviates by $3.2''$ from the refined position given in Grupe (2006). The most likely reason for this difference is that for the X-ray position given in Grupe (2006) only the PC mode data of the first orbit were used. This is due to the burst during the first orbit being placed on one of the bad columns on the XRT CCD, which makes the determination of a position difficult. Figure 1 displays the UVW1 image of the field of GRB 060729. The circle in the top right inserted image is the $3.5''$ XRT error radius of the X-ray position given above.

### 3.2. *BAT Data*

Figure 2 displays the BAT light curves in the 15–25, 25–50 50–100, and 15–100 keV bands (*top to bottom*) with $T_0$ = 2006 July 29 19:12:29 UT (spacecraft clock 175893150.592). GRB 060729 had $T_{90}$ = 115 s (Parsons et al. 2006). Partly the $T_{90}$ is so long because the trigger was on the precursor. After the initial first peak (precursor), which was detected by the BAT and which triggered the observation, the burst drops back down to the background level. However, two giant peaks are observed at about 60 s after the trigger, of which the first is harder than the second. There is a third peak about 120 s after the trigger. This is the peak of which we see the end of the decay in the XRT observation (Fig. 3). For the spectral analysis the BAT data were divided into five bins as listed in Table 1. The first peak is the initial peak the BAT triggered on GRB 060729. As shown in Table 1, the following two peaks, which occur between 70 and 124 s after the burst, are a factor of 3 stronger than the initial peak. The two last peaks (124–190 s after the burst; XRT flare 1 and 2 in Table 1), are also observed simultaneously in the XRT. These data are discussed in the XRT section.

Table 1 lists the results of the spectral analysis of the five peaks. All spectra were fitted by a single–power-law model. The initial peak has a hard spectrum with a 15–150 keV energy spectra index $\beta_{15-150\mathrm{keV}} = 1.05^{+0.42}_{-0.32}$. The two strong peaks between 70–124 s after the burst show interesting spectral behavior. While the first of these peaks (70–88 s after the burst) has a rather hard spectral slope, with $\beta_{15-150\mathrm{keV}} = 0.59 \pm 0.11$, the second of these peaks (88–124 s) was softer, with $\beta_{15-150\mathrm{keV}} = 0.90 \pm 0.11$. The total fluence in the observed 15–150 keV band is $2.7 \times 10^{-6}$ ergs cm$^{-2}$ (Parsons et al. 2006) and $7.2 \times 10^{-6}$ and $1.7 \times 10^{-5}$ ergs cm$^{-2}$ in the rest-frame 1 keV–1 MeV and 1 keV–10 MeV bands, respectively, adding all BAT spectra together (Table 1) and assuming the same power-law spectrum as in the 15–150 keV band without any break. With a redshift of $z = 0.54$ this converts into an isotropic energy in the rest-frame 1 keV–1 MeV and 1 keV–10 MeV band of $E_{\mathrm{iso}} = 6.7 \times 10^{51}$ and $E_{\mathrm{iso}} = 1.6 \times 10^{52}$ ergs, respectively. Because we lack observations of the break energy $E_{\mathrm{break}}$ and the gamma-ray spectrum at higher energies by Konus-*Wind*, the 1 keV–10 MeV band $E_{\mathrm{iso}}$ value is an upper limit of the true isotropic energy.

### 3.3. *X-Ray Data*

#### 3.3.1. *Temporal Analysis*

Figure 3 shows the combined BAT and XRT light curve. The light curve clearly shows that XRT began observing the GRB at the beginning of the fourth peak seen in the BAT. The combined BAT+XRT light curve was constructed as described in O'Brien et al. (2006). Due to the dramatic spectral change within the 3 minutes of the WT observation, we applied an ECF for each individual

TABLE 1
SPECTRAL FITS TO THE BAT DATA

| | | | | FLUX[a] | | | FLUENCE[b] | | |
|---|---|---|---|---|---|---|---|---|---|
| SPECTRUM | $T$ AFTER TRIGGER | $\beta_{15-150\mathrm{keV}}$ | $\chi^2/\nu$ | 15–150 keV | 1 keV–1 MeV[c] | 1 keV–10 MeV[c] | 15–150 keV | 1 keV–1 MeV[c] | 1 keV–10 MeV[c] |
| First peak ..... | 0–10 | $1.05^{+0.42}_{-0.37}$ | 57/56 | $3.2 \times 10^{-8}$ | $1.0 \times 10^{-7}$ | $1.3 \times 10^{-7}$ | $3.2 \times 10^{-7}$ | $1.0 \times 10^{-6}$ | $1.3 \times 10^{-6}$ |
| Second peak..... | 70–88 | $0.59^{+0.11}_{-0.11}$ | 59/56 | $5.8 \times 10^{-8}$ | $1.6 \times 10^{-7}$ | $4.5 \times 10^{-7}$ | $1.0 \times 10^{-6}$ | $2.8 \times 10^{-6}$ | $8.1 \times 10^{-6}$ |
| Third peak..... | 88–124 | $0.90^{+0.11}_{-0.11}$ | 50/56 | $2.8 \times 10^{-8}$ | $7.7 \times 10^{-8}$ | $1.2 \times 10^{-7}$ | $1.0 \times 10^{-6}$ | $2.8 \times 10^{-6}$ | $4.3 \times 10^{-6}$ |
| XRT flare 1 ..... | 124–160 | $1.26^{+1.58}_{-0.86}$ | 49/56 | $2.6 \times 10^{-9}$ | $1.1 \times 10^{-8}$ | $1.3 \times 10^{-8}$ | $9.4 \times 10^{-8}$ | $4.0 \times 10^{-7}$ | $4.7 \times 10^{-7}$ |
| XRT flare 2 ..... | 180–190 | $1.59^{+5.23}_{-1.67}$ | 53/56 | $1.8 \times 10^{-9}$ | $1.5 \times 10^{-8}$ | $1.5 \times 10^{-8}$ | $1.8 \times 10^{-8}$ | $1.5 \times 10^{-7}$ | $1.5 \times 10^{-7}$ |

NOTE.—The BAT data have been divided into five segments as listed in the first column.
[a] The 15–150 keV flux is in units of ergs s$^{-1}$ cm$^{-2}$.
[b] Fluence in units of ergs cm$^{-2}$.
[c] Rest-frame 1 keV–1 MeV (0.65–650 keV observed) and 1 keV–10 MeV (0.65 keV-6.5 MeV observed).

TABLE 2
SPECTRAL ANALYSIS OF THE 21 BINS OF THE *Swift* WT MODE DATA

| | | | | | Single Power Law | | | Blackbody + Power Law | | | | Power Law with Exponential Cutoff | |
|---|---|---|---|---|---|---|---|---|---|---|---|---|---|
| Bin No. | Time | $T_{obs}$ | CR[a] | HR[b] | $N_H$[c] | $\beta_X$ | $\chi^2/\nu$ | $kT$[d] | bb-Flux[e] | $R_{bb}$[f] | $\chi^2/\nu$ | $E_{cutoff}$[g] | $\chi^2/\nu$ |
| 1 | 131 | 1.2 | 919 ± 30 | 0.55 ± 0.06 | ... | ... | ... | ... | ... | ... | ... | ... | ... |
| 2 | 132 | 1.2 | 841 ± 28 | 0.60 ± 0.06 | $4.06^{+1.39}_{-1.15}$ | $1.51^{+0.35}_{-0.31}$ | 21/23 | $0.56^{+0.05}_{-0.04}$ | 7.46 | 2.49 | 16/23 | $0.82^{+0.44}_{-0.08}$ | 15/23 |
| 3 | 133 | 1.4 | 807 ± 27 | 0.51 ± 0.05 | ... | ... | ... | ... | ... | ... | ... | ... | ... |
| 4 | 135 | 1.6 | 737 ± 25 | 0.43 ± 0.05 | $4.51^{+0.88}_{-0.77}$ | $2.10^{+0.29}_{-0.25}$ | 39/32 | $0.45^{+0.04}_{-0.03}$ | 6.13 | 3.46 | 51/32 | $0.78^{+0.36}_{-0.02}$ | 48/32 |
| 5 | 136 | 1.6 | 712 ± 24 | 0.47 ± 0.05 | ... | ... | ... | ... | ... | ... | ... | ... | ... |
| 6 | 138 | 1.8 | 635 ± 22 | 0.42 ± 0.05 | $5.22^{+0.98}_{-0.85}$ | $2.40^{+0.33}_{-0.30}$ | 36/31 | $0.43^{+0.02}_{-0.02}$ | 6.23 | 3.91 | 34/31 | $0.51^{+0.59}_{-0.39}$ | 33/31 |
| 7 | 140 | 2.1 | 579 ± 19 | 0.33 ± 0.04 | ... | ... | ... | ... | ... | ... | ... | ... | ... |
| 8 | 142 | 2.6 | 520 ± 18 | 0.29 ± 0.04 | $4.35^{+0.58}_{-0.53}$ | $2.47^{+0.24}_{-0.21}$ | 39/46 | $0.38^{+0.02}_{-0.02}$ | 5.72 | 4.69 | 45/46 | $0.59^{+0.46}_{-0.25}$ | 45/46 |
| 9 | 145 | 3.1 | 498 ± 16 | 0.25 ± 0.04 | ... | ... | ... | ... | ... | ... | ... | ... | ... |
| 10 | 149 | 4.4 | 380 ± 12 | 0.12 ± 0.04 | $4.70^{+0.65}_{-0.58}$ | $2.99^{+0.32}_{-0.28}$ | 75/50 | $0.31^{+0.02}_{-0.02}$ | 3.60 | 5.48 | 96/50 | $0.50^{+0.3}_{-0.2}$ | 107/50 |
| 11 | 154 | 5.7 | 289 ± 10 | −0.00 ± 0.04 | $3.00^{+0.62}_{-0.56}$ | $2.64^{+0.34}_{-0.30}$ | 29/34 | $0.25^{+0.02}_{-0.02}$ | 2.81 | 7.35 | 30/34 | $0.67^{+0.47}_{-0.09}$ | 33/34 |
| 12 | 161 | 7.3 | 227 ± 7 | −0.07 ± 0.04 | $3.07^{+0.71}_{-0.63}$ | $2.73^{+0.41}_{-0.36}$ | 43/32 | $0.29^{+0.02}_{-0.02}$ | 1.98 | 4.84 | 32/32 | $0.64^{+0.47}_{-0.15}$ | 34/32 |
| 13 | 167 | 6.4 | 258 ± 9 | 0.10 ± 0.04 | $2.29^{+0.60}_{-0.54}$ | $2.04^{+0.33}_{-0.29}$ | 38/32 | $0.27^{+0.03}_{-0.03}$ | 1.45 | 4.77 | 43/32 | $1.15^{+0.64}_{-0.34}$ | 48/32 |
| 14 | 173 | 5.2 | 320 ± 10 | 0.21 ± 0.04 | $3.60^{+0.62}_{-0.56}$ | $2.46^{+0.27}_{-0.24}$ | 40/33 | $0.34^{+0.03}_{-0.02}$ | 3.54 | 4.68 | 39/33 | $0.72^{+0.37}_{-0.05}$ | 37/33 |
| 15 | 179 | 5.4 | 310 ± 10 | 0.15 ± 0.04 | $2.43^{+0.59}_{-0.53}$ | $2.01^{+0.30}_{-0.28}$ | 39/35 | $0.32^{+0.03}_{-0.02}$ | 2.90 | 4.61 | 37/35 | $0.78^{+0.40}_{-0.03}$ | 35/35 |
| 16 | 184 | 5.5 | 301 ± 10 | 0.02 ± 0.04 | $2.97^{+0.67}_{-0.60}$ | $2.57^{+0.38}_{-0.34}$ | 35/34 | $0.26^{+0.02}_{-0.02}$ | 3.28 | 7.52 | 32/34 | $0.58^{+0.56}_{-0.23}$ | 36/34 |
| 17 | 190 | 7.4 | 227 ± 7 | -0.09 ± 0.03 | $3.46^{+0.85}_{-0.76}$ | $3.07^{+0.51}_{-0.46}$ | 55/35 | $0.24^{+0.01}_{-0.01}$ | 3.24 | 8.76 | 40/35 | $0.51^{+0.18}_{-0.13}$ | 45/35 |
| 18 | 199 | 9.4 | 178 ± 5 | -0.26 ± 0.03 | $2.48^{+0.62}_{-0.55}$ | $2.98^{+0.41}_{-0.36}$ | 62/39 | $0.19^{+0.01}_{-0.01}$ | 3.44 | 14.84 | 58/39 | $0.55^{+0.62}_{-0.29}$ | 60/39 |
| 19 | 210 | 14.0 | 127 ± 4 | -0.31 ± 0.03 | $2.34^{+0.63}_{-0.54}$ | $3.07^{+0.42}_{-0.36}$ | 59/38 | $0.18^{+0.01}_{-0.01}$ | 2.84 | 15.40 | 33/38 | $0.51^{+0.69}_{-0.31}$ | 60/38 |
| 20 | 229 | 23.4 | 72 ± 2 | -0.50 ± 0.03 | $1.83^{+0.53}_{-0.44}$ | $3.28^{+0.41}_{-0.35}$ | 72/36 | $0.15^{+0.01}_{-0.01}$ | 2.15 | 18.19 | 38/36 | $0.51^{+0.6}_{-0.5}$ | 76/36 |
| 21 | 296 | 112.0 | 14.8 ± 0.4 | -0.56 ± 0.03 | $0.84^{+0.35}_{-0.30}$ | $2.83^{+0.36}_{-0.32}$ | 64/37 | $0.11^{+0.01}_{-0.01}$ | 0.50 | 15.65 | 52/37 | ... | ... |

NOTE.—For the blackbody plus power-law and the power-law with exponential cutoff model the power-law slope was fixed to $\beta_X = 1.0$. For the blackbody plus power-law model the absorption parameter was fixed to the Galactic value ($4.82 \times 10^{20}$ cm$^{-2}$; Dickey & Lockman 1990).

[a] Count rate in units of counts s$^{-1}$.
[b] The hardness ratio is defined as HR = (hard − soft)/(hard + soft), where "soft" and "hard" are the photons in the 0.3–1.0 and 1.0–10.0 keV band, respectively.
[c] The column density $N_H$ is given in units of $10^{21}$ cm$^{-2}$.
[d] Blackbody temperature in units of keV.
[e] The fluxes are given in units of $10^{-9}$ ergs s$^{-1}$ cm$^{-2}$.
[f] Blackbody radius $R_{bb}$ given in units of $10^{12}$ cm.
[g] The break energy is given in units of keV.

bin assuming a power-law model corrected for absorption with the parameters listed in Table 2. However, for the BAT data we applied only one ECF, which reflects the main spectrum.

Figure 4 displays the *Swift* XRT light curve, with WT mode data as triangles and PC mode data as crosses. The vertical dashed lines in the figure mark the start and end times of the *XMM-Newton* observations. The general behavior of the light curve can be described as follows: after the initial steep decay with a decay slope $\alpha_1 = 5.11 \pm 0.22$ the light curve flattens at $T_{break,1} = 530 \pm 25$ s, with a decay slope $\alpha_2 = 0.14 \pm 0.02$. At $T_{break,2} = 56.8 \pm 10$ ks the light curve of the afterglow breaks again and continues decaying with a decay slope $\alpha_3 = 1.29 \pm 0.03$. The definitions of the decay slopes follow the descriptions given in Nousek et al. (2006) and Zhang et al. (2006). We do not detect a jet break even 125 days after the burst. The last 3 $\sigma$ detection of the X-ray afterglow was obtained between 2006 November 21 to December 1, with a total exposure time of 69.9 ks. The afterglow continued to be observed by *Swift* until December 27, for a total of 63.5 ks. However, these observations were interrupted by several new bursts, and at the end only a 3 $\sigma$ upper limit of $2.1 \times 10^{-14}$ ergs s$^{-1}$ cm$^{-2}$ could be obtained. It was dropped from the *Swift* schedule after 2006 December 27 because it was not detectable anymore with the XRT within a reasonable amount of observing time.

### 3.3.2. *Spectral Analysis*

*Dramatic spectral change at the beginning.*—In order to examine the spectral behavior in more detail, source and background spectra were created for each bin, except for the first 10 bins ($T - T_0 = 130$–$150$ s). The WT mode data were divided into 21 bins with 1000 source photons in each bin. Because of the high count rate at the beginning of the observations we applied the method as described in Romano et al. (2006) to avoid the effects of pileup. However, this procedure reduced significantly the number of source photons in each single spectrum. We therefore

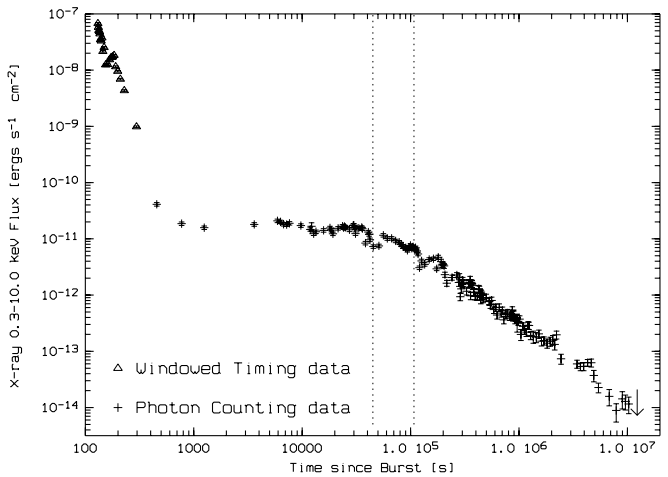


FIG. 4.—*Swift* XRT light curve of the WT (*triangles*) and PC (*crosses*) mode. The downward arrow marks the 3 $\sigma$ upper limit at the end of the *Swift* observations. This upper limit contains a total exposure time of 63.5 ks obtained between 2006 December 8 and December 27. The dotted vertical lines mark the start and end times of the *XMM-Newton* observation.

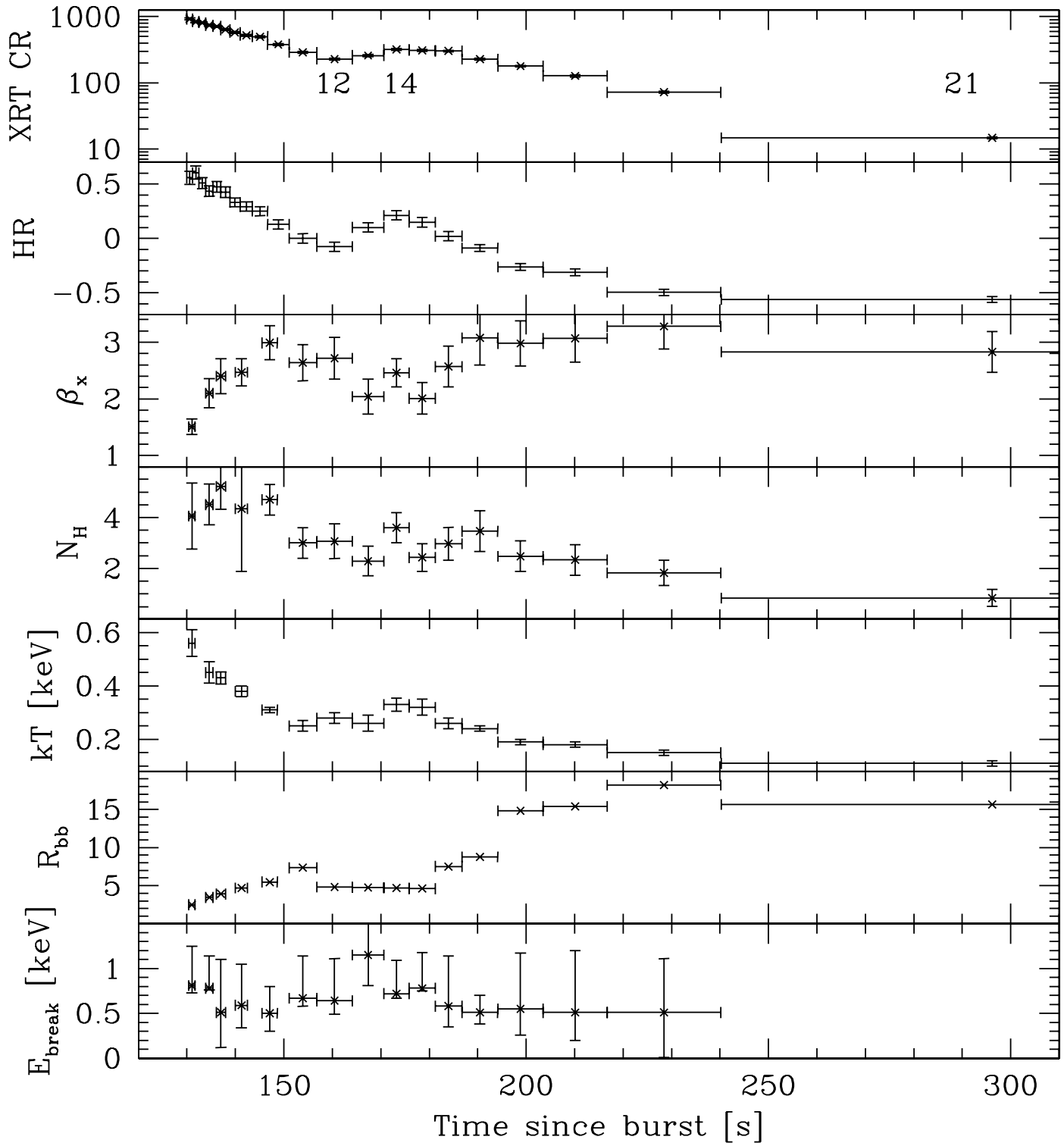


FIG. 5.—*Swift* XRT WT mode light curve. The panels display (*top to bottom*) the XRT count rate (in units of counts $s^{-1}$), the hardness ratio (see text for definition), the X-ray spectral slope $\beta_X$ of a single–power-law fit, the free-fit column density $N_H$ in units of $10^{21}$ $cm^{-2}$, the blackbody temperature $kT$, the blackbody radius $R_{bb}$ (in units of $10^{12}$ cm), and the cutoff energy $E_{break}$ of a power law with exponential cutoff. All these fit parameters are listed in Table 2. The numbers in the top panel mark the bins that were used for the spectra shown in Fig. 6.

combined two bins into one for bins 1+2, 3+4, 5+6, 7+8, and 9+10 to increase the S/N.

Each of the 16 spectra were fitted by an absorbed single–power-law, blackbody plus power-law, and a power-law with exponential cutoff model. The results of these spectral fits are listed in Table 2. Figure 5 shows plots of the WT mode data as follows: (*top to bottom*) count rate, hardness ratio, X-ray spectral slope $\beta_X$ from an absorbed single–power-law fit with a free-fit absorption column density $N_H$, blackbody temperature $kT$ (in keV) from the blackbody plus power-law fit, blackbody radius[13] $R_{bb}$, and the break energy $E_{break}$ of a power-law with exponential

[13] The blackbody radii were derived for each bin from the relation $L = 4\pi R_{bb}^2 \sigma T^4$, where $\sigma$ is the Stefan-Boltzmann constant.

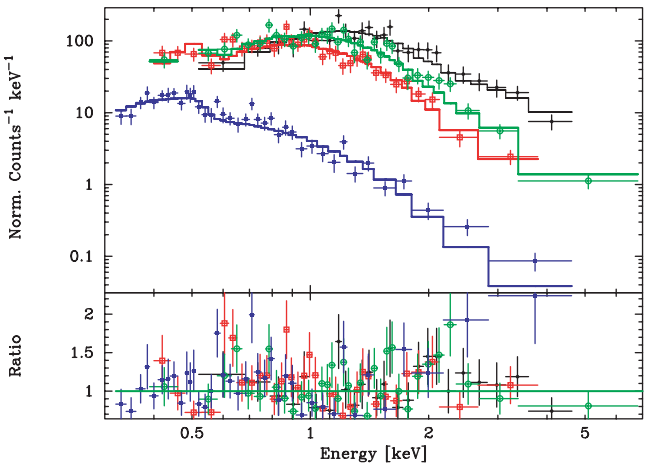


FIG. 6.—*Swift* XRT WT spectra of bins 1+2 (*black filled circles*), 12 (*red open squares*), 14 (*green open circles*), and 21 (*blue filled squares*) fitted by absorbed single power laws as given in Table 2. The numbers refer to the bins as shown in Fig. 5.

cutoff model. The hardness ratio changes from HR = 0.6 at the beginning of the observation to HR = −0.56 at the end, indicating a dramatic evolution in the X-ray spectrum within 2 minutes of observing time, which translates into 1.3 minutes in the rest frame.

While the spectra during the first 20 s of the WT mode observation are well fitted by a single–power-law model, after about 150 s after the burst the data are better fit by a blackbody plus power-law spectrum. For the absorbed power-law fits, all parameters were left free. We found that while the spectra at the beginning of the observation were rather hard, with $\beta_X = 1.5$ and $N_H = 4 \times 10^{21}$ cm$^{-2}$, the spectra became very soft, with $\beta_X \sim 3.0$ and $N_H = 1 \times 10^{21}$ cm$^{-2}$. Note that the absorption column density $N_H$ decreases, while the energy spectral index $\beta_X$ becomes steeper—the opposite of what is expected if the spectral slope and the absorption column density were just linked in the fitting program. However, note that especially during the later bins, the spectra are not well fit by a single power law and do require more complicated models.

For the blackbody plus power-law model, the absorption parameter was fixed at the Galactic value ($4.82 \times 10^{20}$ cm$^{-2}$; Dickey & Lockman 1990) and the hard energy spectral slope a $\beta_X = 1.0$. The blackbody temperature changes dramatically from $kT = 0.56$ keV at the beginning of the XRT WT observation to 0.11 keV at the end, accompanied by an increase of the blackbody radius from $2.5 \times 10^{12}$ to $16 \times 10^{12}$ cm. Fitting the data with an absorbed blackbody plus power-law model with the absorption column density at $z = 0$ set to the Galactic value and at $z = 0.54$ to $1 \times 10^{21}$ cm$^{-2}$ (see the discussion about the *XMM-Newton* spectral analysis) results in similar values for the temperature. The only differences are that the temperatures tend to be lower by 40 eV and the normalizations are higher.

The prompt emission of GRBs is often fitted by a Band function (Band et al. 1993). We also tried a power-law model with exponential cutoff, a surrogate for the Band model that has the advantage of using fewer parameters than the Band model. In order to obtain better constraints we fixed the absorption column to the Galactic value. As listed in Table 2, typically the power-law model with exponential cutoff does not show improvement over the single–power-law or the blackbody plus power-law models.

The change in the X-ray spectra is also displayed in Figure 6, which shows the spectra of bins 1, 12, 14, and 21. Bin 12 is the bin before the small flare at 170 s after the burst, and bin 14 is the peak of that flare.

*Later PC mode data*.—All PC mode data can be fitted by a power-law model with a energy spectral slope $\beta_X = 1.2$ and an absorption column density of about $1.5 \times 10^{21}$ cm$^{-2}$. This absorption column density is significantly above the Galactic value. The intrinsic absorption column density at the redshift $z = 0.54$ is $1.9 \pm 0.4 \times 10^{21}$ cm$^{-2}$. Table 3 lists the XRT PC mode observations at 20–40 ks after the burst and at 200 ks after the burst, so before and after the *XMM* observation. The fits to these data suggest no significant spectral variability before or after the break in the X-ray light curve around 60 ks after the burst.

*The XMM-Newton observations*.—The combined spectra of the *XMM-Newton* EPIC pn and MOS and *Swift* XRT data are shown in Figure 7. The XRT data were selected between 44,900 and 107,500 s after the burst. The details of the spectral fits to these data are summarized in Table 3. At these late times, the X-ray spectra were well fitted by absorbed single–power-law models. However, as a check the spectra were fitted also by a blackbody plus power-law model, although at these late times the power-law component dominates the spectra. Therefore, we only discuss the absorbed power-law model fits as listed in Table 3.

The obvious difference between the *Swift* XRT and *XMM-Newton* pn and MOS data is the much higher value of the absorption column density. From the free fit absorption column density at $z = 0$ we measured an absorption column density $N_H = 15.7 \times 10^{20}$ cm$^{-2}$ in the *Swift* XRT data. This value is about twice as high as what is measured from the *XMM-Newton* EPIC pn and MOS spectra. The EPIC pn is well calibrated to energies below 0.2 keV

TABLE 3
SPECTRAL FITS TO THE *Swift* XRT PC MODE AND *XMM* EPIC pn AND MOS DATA

| Detector | $N_H$[a] | $\beta_X$ | $\chi^2/\nu$ | $N_{H,intr}$[b] | $\beta_X$ | $\chi^2/\nu$ |
|---|---|---|---|---|---|---|
| *Swift* XRT (20–40 ks after burst) | $16.83^{+2.30}_{-2.17}$ | $1.21^{+0.10}_{-0.09}$ | 87/103 | $21.57^{+4.22}_{-3.92}$ | $1.12 \pm 0.08$ | 88/103 |
| *Swift* XRT (44.9–107.5 ks after burst) | $15.72^{+2.22}_{-2.10}$ | $1.19^{+0.09}_{-0.09}$ | 134/120 | $19.20^{+4.00}_{-3.72}$ | $1.11^{+0.08}_{-0.07}$ | 134/120 |
| *Swift* XRT (200 ks after burst) | $14.65^{+6.22}_{-5.55}$ | $1.17^{+0.25}_{-0.22}$ | 33/25 | $17.46^{+11.10}_{-9.65}$ | $1.10^{+0.20}_{-0.19}$ | 33/25 |
| XMM EPIC pn | $8.58^{+0.20}_{-0.20}$ | $1.12^{+0.01}_{-0.01}$ | 1159/1149 | $7.79^{+0.39}_{-0.38}$ | $1.11^{+0.01}_{-0.01}$ | 1124/1149 |
| XMM MOS1+MOS2 | $9.33^{+0.33}_{-0.32}$ | $1.04^{+0.02}_{-0.02}$ | 937/800 | $8.23^{+0.59}_{-0.58}$ | $1.01^{+0.01}_{-0.01}$ | 929/800 |
| XMM MOS 1+2+*Swift* XRT | $9.54^{+0.32}_{-0.32}$ | $1.05^{+0.02}_{-0.02}$ | 1106/920 | $8.61^{+0.06}_{-0.06}$ | $1.02^{+0.01}_{-0.01}$ | 1097/920 |
| XMM pn+MOS1+2+*Swift* XRT[b] | $8.57^{+0.17}_{-0.17}$ | $1.08^{+0.01}_{-0.01}$ | 2599/2071 | $7.55^{+0.03}_{-0.03}$ | $1.06^{+0.01}_{-0.01}$ | 2508/2071 |

NOTE.—*XMM* observed the afterglow between 44.9–107.5 ks after the burst.
[a] The column density $N_H$ at $z = 0$ is given in units of $10^{20}$ cm$^{-2}$.
[b] Intrinsic column density $N_{H,intr}$ at the redshift of the burst, $z = 0.54$, is given in units of $10^{20}$ cm$^{-2}$. The absorption column density at $z = 0$ is set to the Galactic value, $4.82 \times 10^{20}$ cm$^{-2}$.

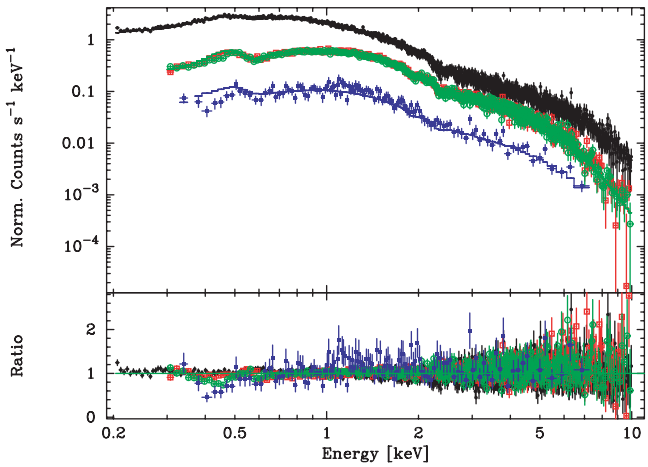


FIG. 7.—Absorbed-power-law model fits with $N_{\rm H} = 8.57 \times 10^{20}$ cm$^{-2}$ and $\beta_{\rm X} = 1.08$, as listed in Table 3, to the *XMM-Newton* EPIC pn (*black filled circles*), MOS1 (*red open squares*), MOS2 (*green open circles*), and *Swift* XRT PC mode (*blue filled squares*) spectra. The *Swift* XRT data were selected between 44.9 and 107.5 ks after the burst, simultaneous with the *XMM-Newton* observation.

(e.g., Haberl et al. 2003). We also applied the `gain fit` model within XSPEC, but it did not remove the discrepancy. This discrepancy maybe due to problems with the *Swift* XRT bias maps during the time period between 2006 July 21 and August 3. This bias map problem caused an offset in the gain and therefore compromised the spectral analysis of *Swift* XRT PC mode data during that time. However, this gain shift does not affect the early *Swift* XRT WT mode data. Due to the better response of the EPIC pn at lower energies we consider the absorption column densities measured by the EPIC pn the most reliable. With the redshift of the burst at $z = 0.54$ we can also use the X-ray spectra to determine the intrinsic absorption column density at the location of the afterglow. The intrinsic column densities of all fits are in the order of $1 \times 10^{21}$ cm$^{-2}$, except for the *Swift* XRT data, which again show an absorption column density about twice as high. As we show later in § 3.5, the absorption column density of $1 \times 10^{21}$ cm$^{-2}$ is in good agreement with what can be derived from the spectral energy distribution (SED) of the afterglow.

In addition to the EPIC pn and MOS data we also analyzed the two RGS spectra. We found that the analysis of the RGS continuum spectra agrees within the errors with the pn and MOS data. We did not find any obvious emission or absorption features in the RGS spectra.

### 3.4. *UV/Optical Data Analysis*

The magnitudes resulting from the UVOT data analysis are listed in Table 4. Figure 8 shows the results of the UVOT photometry in comparison with the XRT. UVOT was able to follow the afterglow in all six filters up to 9 days after the burst. In UVW1 the afterglow was followed up 31 days after the burst, which translates into 20 days in the rest frame. This is one of the longest intervals *Swift*'s UVOT has ever detected an afterglow in the optical/UV. Only GRBs 060218 (Campana et al. 2006) and 060614 (Mangano et al. 2007) were detected at slightly later observed times than GRB 060729.

In all bands, XRT as well as in all six UVOT filters, a significant break occurs in the light curve. Table 5 lists the decay slopes $\alpha_2$ and $\alpha_3$ before and after the break time $T_{\rm break}$. Within the errors all break times seem to occur at about 50 ks after the burst (33 ks in the rest frame), with the earliest break in *B* at about 30 ks and the later breaks at shorter wavelengths. However, considering the uncertainties in the decay slopes, this is all consistent with an achromatic break. Note that due to a rebrightening of the afterglow at about 20 ks seen in X-rays and all six UVOT filters the determination of $\alpha_2$ is rather uncertain. In *B* the afterglow decays the slowest with $\alpha_3 = 0.98$. The decay slopes at shorter wavelengths are steeper with $\alpha_3 \approx= 1.3$. Note that the flatter slope in the *B* filter is caused by a rebrightening at about 200 ks that is not seen in the other filters. By limiting the analysis to data only up to 200 ks the decay slope is $\alpha_3 = 1.17 \pm 0.16$, which is consistent with the decay slopes seen in the other filters. The rebrightening in *B* at about 200 ks after the burst seems to be real. We checked for any strong variability in the background but could not detect any at that time. The decay slopes $\alpha_2$ and $\alpha_3$ are consistent with the decay slopes reported by Quimby & Rykoff (2006) and Cobb & Bailyn (2006).

Figure 9 displays the UVOT white and *V* and XRT light curves of the first orbit. The UVOT data of this period are listed in Table 6. The left panel of Figure 9 displays the UVOT white filter event mode and XRT WT mode data. The UVOT white filter data were grouped into 10 s bins. The first UVOT white points show a decay similar to the XRT WT light curve. However, after these few points the UVOT white light curve flattens, which agrees with the flare seen in the XRT data at 170 s after the burst. At about 200 s after the burst the afterglow starts to become brighter in the UVOT white, while it is still decaying in the X-ray.

The right panel of Figure 9 shows the UVOT *V* event mode data and the XRT PC mode data of the first orbit. The UVOT V data were grouped in 25 s bins and the XRT PC mode data with 25 source photons bin$^{-1}$. The UVOT *V* light curve shows the afterglow fairly constant at about 17.5 mag, while the XRT PC mode light curves shows an initial decay until about 600 s and flattens after that.

The *XMM-Newton* optical monitor observations are summarized in Table 7. While the *U* filter results agree well with the UVOT *U* data as listed in Table 4, there is a discrepancy in the UVW1 and UVM2 filters. There may be three explanations for this discrepancy: (1) the OM and UVOT UV filter sets have different filter transmission; (2) the OM suffers from significantly higher level of scattered light than the UVOT; and (3) the extraction radius of the automated OM software is 12″, which is too large for an accurate analysis of the UV data due to the bright star (see UVOT section). The brightening of the afterglow in the last OM UVM2 observation at 101 ks after the burst is most likely due to a bad subtraction of the background within the automatic OM data reduction software.

### 3.5. *Spectral Energy Distribution*

As shown in section 3.4 the long-term light curves in all six UVOT filters and in X-rays do follow the same decay slope with similar break times at about 50 ks after the burst. In order to check this we determined SEDs of the afterglow at 800 s, 20, 100, and 500 ks, with exposure times in the XRT of 400 s, 1.8, 3.3, and 4.8 ks, respectively. Figure 10 displays these four SEDs. These times are also marked in Figure 8. These times were picked to represent the SEDs of the earliest and latest time possible when the afterglow was detected in all six UVOT filters and shortly before and after the break. All fluxes in all six UVOT filters and the XRT were calculated according to the light curves. There seem to be no obvious changes in the SEDs, besides the changes in the fluxes, over time. Another measure of any changes in the SEDs over time is the optical/UV to X-ray spectral slope or X-ray loudness[14] $\beta_{\rm oX}$. For the afterglow of GRB 060729 we measured

[14] The X-ray loudness is defined by Tananbaum et al. (1979) as $\beta_{\rm oX} = -0.384 \log (f_{\rm 2keV}/f_{\rm 2500\AA})$.

TABLE 4

CENTRAL TIMES, EXPOSURE TIMES, AND APERTURE-CORRECTED MAGNITUDES OF THE UVOT LIGHT CURVES

| | *V* FILTER | | | *B* FILTER | | | *U* FILTER | | | UVW1 FILTER | | | UVM2 FILTER | | | UVW2 FILTER | | |
|---|---|---|---|---|---|---|---|---|---|---|---|---|---|---|---|---|---|---|
| BIN NO. | Time[a] | $T_{exp}$[b] | Mag | Time[a] | $T_{exp}$[b] | Mag | Time[a] | $T_{exp}$[b] | Mag | Time[a] | $T_{exp}$[b] | Mag | Time[a] | $T_{exp}$[b] | Mag | Time[a] | $T_{exp}$[b] | Mag |
| 1 | 120 | 9 | 17.07 ± 0.31 | 715 | 10 | 18.27 ± 0.38 | 696 | 20 | 16.48 ± 0.12 | 673 | 20 | 16.92 ± 0.20 | 649 | 18 | 16.81 ± 0.24 | 749 | 20 | 17.54 ± 0.25 |
| 2 | 440 | 390 | 17.37 ± 0.06 | 1451 | 20 | 18.03 ± 0.23 | 844 | 20 | 16.88 ± 0.15 | 820 | 20 | 16.89 ± 0.20 | 796 | 20 | 17.57 ± 0.33 | 1489 | 20 | 16.95 ± 0.19 |
| 3 | 773 | 19 | 17.36 ± 0.26 | 1609 | 20 | 18.10 ± 0.26 | 1427 | 20 | 16.85 ± 0.16 | 1403 | 20 | 17.47 ± 0.26 | 1379 | 20 | 17.12 ± 0.26 | 1647 | 20 | 17.39 ± 0.23 |
| 4 | 1164 | 393 | 17.32 ± 0.06 | 1767 | 20 | 18.26 ± 0.30 | 1585 | 20 | 16.85 ± 0.15 | 1561 | 20 | 17.31 ± 0.24 | 1537 | 20 | 16.85 ± 0.23 | 1805 | 19 | 16.92 ± 0.19 |
| 5 | 1513 | 19 | 17.45 ± 0.32 | 6224 | 197 | 18.45 ± 0.10 | 1743 | 20 | 16.49 ± 0.13 | 1719 | 20 | 17.14 ± 0.23 | 1695 | 20 | 16.75 ± 0.22 | 6634 | 197 | 17.70 ± 0.09 |
| 6 | 1671 | 19 | 17.16 ± 0.24 | 7657 | 197 | 18.45 ± 0.11 | 6020 | 197 | 17.52 ± 0.07 | 5815 | 197 | 17.55 ± 0.09 | 1850 | 13 | 17.63 ± 0.45 | 7998 | 63 | 17.86 ± 0.17 |
| 7 | 1829 | 19 | 17.55 ± 0.34 | 12919 | 134 | 18.68 ± 0.14 | 7452 | 197 | 17.54 ± 0.07 | 7247 | 197 | 17.62 ± 0.09 | 7043 | 197 | 17.80 ± 0.12 | 11878 | 751 | 18.08 ± 0.06 |
| 8 | 6838 | 197 | 18.10 ± 0.16 | 18042 | 211 | 17.86 ± 0.06 | 12778 | 134 | 17.89 ± 0.11 | 12568 | 268 | 18.09 ± 0.10 | 13880 | 377 | 17.76 ± 0.09 | 13266 | 537 | 18.17 ± 0.07 |
| 9 | 13613 | 134 | 18.38 ± 0.25 | 23824 | 211 | 17.84 ± 0.06 | 17822 | 211 | 16.91 ± 0.05 | 17495 | 422 | 17.11 ± 0.05 | 19550 | 600 | 17.07 ± 0.05 | 18585 | 844 | 17.36 ± 0.04 |
| 10 | 19128 | 211 | 17.33 ± 0.09 | 29606 | 211 | 17.78 ± 0.06 | 23603 | 211 | 17.20 ± 0.06 | 23276 | 422 | 17.23 ± 0.05 | 25338 | 599 | 17.20 ± 0.05 | 24367 | 845 | 17.52 ± 0.04 |
| 11 | 24911 | 211 | 17.73 ± 0.11 | 35388 | 211 | 18.14 ± 0.08 | 29387 | 211 | 17.17 ± 0.06 | 29059 | 422 | 17.22 ± 0.05 | 31109 | 600 | 17.37 ± 0.06 | 30149 | 844 | 17.51 ± 0.04 |
| 12 | 30692 | 211 | 17.53 ± 0.10 | 41205 | 208 | 18.12 ± 0.08 | 35167 | 211 | 17.20 ± 0.06 | 34840 | 422 | 17.35 ± 0.05 | 36892 | 599 | 17.40 ± 0.06 | 35931 | 845 | 17.64 ± 0.04 |
| 13 | 36475 | 211 | 17.98 ± 0.13 | 47494 | 147 | 18.22 ± 0.09 | 40989 | 207 | 17.26 ± 0.06 | 40666 | 415 | 17.35 ± 0.05 | 42681 | 587 | 17.45 ± 0.06 | 41738 | 829 | 17.76 ± 0.05 |
| 14 | 42273 | 207 | 17.86 ± 0.13 | 56873 | 129 | 18.31 ± 0.11 | 47340 | 147 | 17.18 ± 0.07 | 47109 | 296 | 17.24 ± 0.06 | 48550 | 416 | 17.25 ± 0.06 | 47877 | 592 | 17.56 ± 0.05 |
| 15 | 48259 | 147 | 17.47 ± 0.11 | 67943 | 42 | 18.94 ± 0.33 | 53746 | 83 | 17.32 ± 0.10 | 52836 | 183 | 17.36 ± 0.08 | 54427 | 229 | 17.63 ± 0.10 | 54050 | 330 | 17.78 ± 0.08 |
| 16 | 54265 | 83 | 18.12 ± 0.26 | 75864 | 211 | 18.77 ± 0.12 | 62872 | 69 | 17.24 ± 0.11 | 58802 | 385 | 17.60 ± 0.06 | 63155 | 177 | 17.93 ± 0.14 | 62989 | 277 | 18.18 ± 0.10 |
| 17 | 63099 | 69 | 18.29 ± 0.35 | 81646 | 211 | 18.88 ± 0.13 | 69860 | 211 | 17.75 ± 0.08 | 64698 | 436 | 17.76 ± 0.07 | 100500 | 603 | 18.66 ± 0.11 | 76105 | 249 | 18.14 ± 0.10 |
| 18 | 91349 | 223 | 18.68 ± 0.22 | 87426 | 211 | 18.96 ± 0.14 | 75644 | 211 | 17.84 ± 0.08 | 69533 | 422 | 17.85 ± 0.07 | 106280 | 599 | 18.57 ± 0.11 | 82086 | 640 | 18.48 ± 0.08 |
| 19 | 100080 | 211 | 18.45 ± 0.22 | 93208 | 211 | 18.72 ± 0.11 | 81426 | 211 | 18.07 ± 0.10 | 75315 | 423 | 17.93 ± 0.07 | 112060 | 597 | 18.58 ± 0.11 | 87970 | 846 | 18.54 ± 0.07 |
| 20 | 105860 | 211 | 18.87 ± 0.28 | 98988 | 211 | 19.11 ± 0.15 | 87206 | 211 | 17.98 ± 0.10 | 81097 | 423 | 18.05 ± 0.08 | 117840 | 600 | 18.52 ± 0.10 | 93752 | 846 | 18.84 ± 0.08 |
| 21 | 111650 | 211 | 18.49 ± 0.19 | 104770 | 211 | 19.02 ± 0.13 | 92987 | 211 | 18.03 ± 0.10 | 86877 | 423 | 18.17 ± 0.08 | 123630 | 600 | 18.90 ± 0.13 | 99532 | 847 | 18.79 ± 0.08 |
| 22 | 117430 | 211 | 19.03 ± 0.32 | 110560 | 211 | 18.84 ± 0.13 | 98767 | 211 | 18.40 ± 0.12 | 92658 | 423 | 18.35 ± 0.09 | 129410 | 601 | 18.81 ± 0.12 | 105320 | 846 | 18.68 ± 0.07 |
| 23 | 123210 | 211 | 18.40 ± 0.20 | 116340 | 211 | 19.18 ± 0.16 | 104550 | 211 | 18.23 ± 0.11 | 98438 | 423 | 18.33 ± 0.09 | 135340 | 294 | 18.79 ± 0.17 | 111100 | 846 | 18.74 ± 0.08 |
| 24 | 128990 | 211 | 18.92 ± 0.27 | 122120 | 211 | 19.62 ± 0.23 | 110340 | 211 | 18.50 ± 0.14 | 104230 | 423 | 18.53 ± 0.10 | 146960 | 342 | 18.99 ± 0.19 | 116880 | 846 | 18.87 ± 0.08 |
| 25 | 135120 | 111 | 18.77 ± 0.38 | 127900 | 211 | 19.32 ± 0.17 | 116120 | 211 | 18.33 ± 0.12 | 110010 | 423 | 18.52 ± 0.10 | 195280 | 737 | 19.62 ± 0.20 | 122660 | 845 | 19.05 ± 0.09 |
| 26 | 158090 | 156 | 19.36 ± 0.56 | 140600 | 225 | 19.37 ± 0.19 | 121900 | 211 | 18.60 ± 0.16 | 115790 | 423 | 18.56 ± 0.10 | 204280 | 189 | 19.48 ± 0.11 | 128450 | 845 | 19.05 ± 0.09 |
| 27 | 226950 | 941 | 19.82 ± 0.29 | 154780 | 180 | 19.77 ± 0.30 | 127680 | 211 | 18.43 ± 0.12 | 121570 | 422 | 18.63 ± 0.11 | 235840 | 471 | 19.84 ± 0.29 | 134830 | 445 | 19.07 ± 0.13 |
| 28 | 319820 | 1374 | 20.22 ± 0.34 | 168380 | 211 | 19.66 ± 0.24 | 134430 | 110 | 18.46 ± 0.17 | 127360 | 423 | 18.76 ± 0.11 | 288290 | 1550 | 19.86 ± 0.16 | 146750 | 522 | 18.84 ± 0.11 |
| 29 | 576790 | 5531 | 21.04 ± 0.40 | 174170 | 209 | 20.00 ± 0.32 | 146620 | 178 | 19.08 ± 0.25 | 137350 | 412 | 18.79 ± 0.12 | 331760 | 2240 | 20.21 ± 0.18 | 168860 | 729 | 19.32 ± 0.11 |
| 30 | 897975 | 2368 | 3σul=20.92 | 179940 | 211 | 20.00 ± 0.32 | 156590 | 211 | 18.64 ± 0.15 | 145550 | 291 | 18.76 ± 0.14 | 397970 | 3140 | 20.33 ± 0.16 | 174710 | 839 | 19.20 ± 0.10 |
| 31 | ... | ... | ... | 194290 | 275 | 19.68 ± 0.20 | 168160 | 211 | 18.70 ± 0.15 | 150480 | 423 | 18.78 ± 0.12 | 487880 | 2980 | 20.59 ± 0.20 | 180340 | 556 | 19.31 ± 0.13 |
| 32 | ... | ... | ... | 206460 | 273 | 19.29 ± 0.15 | 173950 | 209 | 18.84 ± 0.16 | 154560 | 456 | 18.94 ± 0.12 | 663250 | 8830 | 21.68 ± 0.30 | 194650 | 1100 | 19.60 ± 0.11 |
| 33 | ... | ... | ... | 319120 | 1374 | 20.11 ± 0.14 | 179720 | 211 | 19.09 ± 0.21 | 162860 | 261 | 19.18 ± 0.19 | 926689 | 3976 | 3σul=21.96 | 206810 | 1092 | 19.51 ± 0.10 |
| 34 | ... | ... | ... | 449360 | 2304 | 20.38 ± 0.13 | 194150 | 275 | 18.82 ± 0.13 | 167830 | 423 | 19.04 ± 0.13 | ... | ... | ... | 218500 | 8795 | 19.52 ± 0.12 |
| 35 | ... | ... | ... | 662500 | 3619 | 21.23 ± 0.20 | 206310 | 273 | 19.03 ± 0.16 | 173630 | 420 | 18.98 ± 0.13 | ... | ... | ... | 250410 | 1111 | 19.84 ± 0.13 |
| 36 | ... | ... | ... | 897470 | 2368 | 21.48 ± 0.29 | 221160 | 280 | 19.35 ± 0.22 | 179390 | 423 | 19.20 ± 0.15 | ... | ... | ... | 287670 | 2200 | 20.16 ± 0.11 |
| 37 | ... | ... | ... | ... | ... | ... | 253230 | 361 | 19.57 ± 0.23 | 193930 | 549 | 19.21 ± 0.12 | ... | ... | ... | 331140 | 3288 | 20.59 ± 0.13 |
| 38 | ... | ... | ... | ... | ... | ... | 318970 | 1374 | 19.75 ± 0.13 | 206100 | 545 | 19.37 ± 0.14 | ... | ... | ... | 397340 | 4561 | 20.57 ± 0.11 |

TABLE 4—*Continued*

| | *V* Filter | | | *B* Filter | | | *U* Filter | | | UVW1 Filter | | | UVM2 Filter | | | UVW2 Filter | | |
|---|---|---|---|---|---|---|---|---|---|---|---|---|---|---|---|---|---|---|
| Bin No. | Time[a] | $T_{exp}$[b] | Mag | Time[a] | $T_{exp}$[b] | Mag | Time[a] | $T_{exp}$[b] | Mag | Time[a] | $T_{exp}$[b] | Mag | Time[a] | $T_{exp}$[b] | Mag | Time[a] | $T_{exp}$[b] | Mag |
| 39..... | ... | ... | ... | ... | ... | ... | 449220 | 2304 | 20.39 ± 0.16 | 220980 | 559 | 19.37 ± 0.15 | ... | ... | ... | 487280 | 4656 | 20.99 ± 0.14 |
| 40..... | ... | ... | ... | ... | ... | ... | 662390 | 3622 | 21.55 ± 0.35 | 286960 | 1100 | 19.77 ± 0.14 | ... | ... | ... | 662770 | 13555 | 21.45 ± 0.12 |
| 41..... | ... | ... | ... | ... | ... | ... | 897363 | 2368 | 3σul=21.58 | 330430 | 1648 | 19.93 ± 0.13 | ... | ... | ... | 897780 | 9498 | 22.02 ± 0.23 |
| 42..... | ... | ... | ... | ... | ... | ... | ... | ... | ... | 396620 | 2276 | 20.09 ± 0.11 | ... | ... | ... | 1099600 | 13675 | 22.43 ± 0.29 |
| 43..... | ... | ... | ... | ... | ... | ... | ... | ... | ... | 486600 | 2323 | 20.29 ± 0.13 | ... | ... | ... | 1487290 | 17912 | 3σul=23.04 |
| 44..... | ... | ... | ... | ... | ... | ... | ... | ... | ... | 662230 | 7331 | 21.20 ± 0.15 | ... | ... | ... | ... | ... | ... |
| 45..... | ... | ... | ... | ... | ... | ... | ... | ... | ... | 897220 | 4748 | 21.20 ± 0.18 | ... | ... | ... | ... | ... | ... |
| 46..... | ... | ... | ... | ... | ... | ... | ... | ... | ... | 1012900 | 17014 | 21.65 ± 0.15 | ... | ... | ... | ... | ... | ... |
| 47..... | ... | ... | ... | ... | ... | ... | ... | ... | ... | 1614900 | 12901 | 21.82 ± 0.22 | ... | ... | ... | ... | ... | ... |
| 48..... | ... | ... | ... | ... | ... | ... | ... | ... | ... | 1697900 | 14706 | 22.46 ± 0.32 | ... | ... | ... | ... | ... | ... |
| 49..... | ... | ... | ... | ... | ... | ... | ... | ... | ... | 1874500 | 24764 | 22.68 ± 0.27 | ... | ... | ... | ... | ... | ... |
| 50..... | ... | ... | ... | ... | ... | ... | ... | ... | ... | 2091400 | 20552 | 22.11 ± 0.20 | ... | ... | ... | ... | ... | ... |
| 51..... | ... | ... | ... | ... | ... | ... | ... | ... | ... | 2394800 | 39794 | 22.63 ± 0.38 | ... | ... | ... | ... | ... | ... |
| 52..... | ... | ... | ... | ... | ... | ... | ... | ... | ... | 3431882 | 44673 | σul=22.76 | ... | ... | ... | ... | ... | ... |

[a] The times mark the middle of the time bin in s after the burst.
[b] The exposure times $T_{exp}$ are given in seconds.

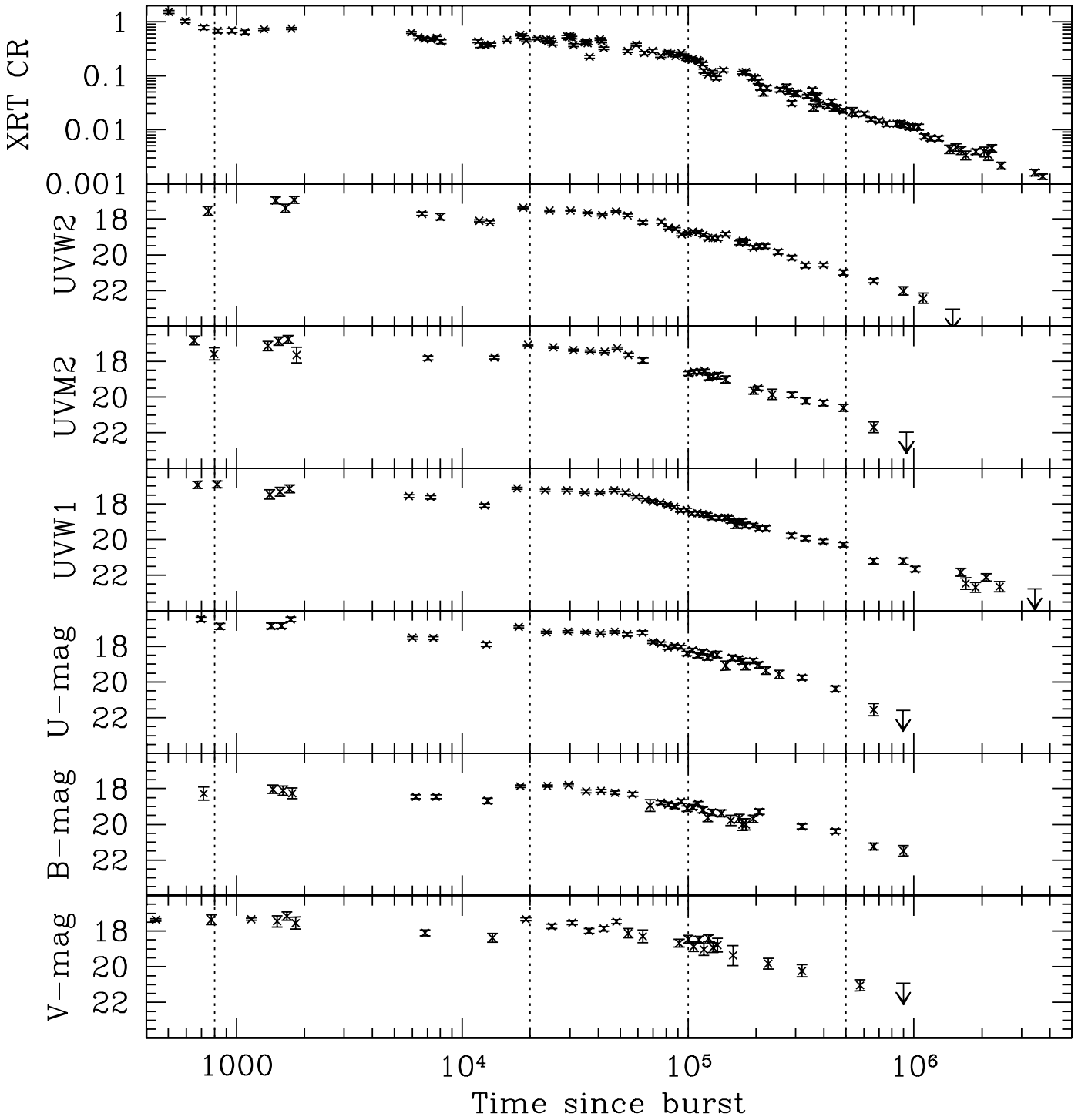


FIG. 8.—*Swift* UVOT and XRT PC mode light curves, with the XRT light curve on the top and the UVOT light curves starting with UVW2 on the top and $V$ on the bottom. The downward arrows mark the 3 $\sigma$ upper limits, as listed in Table 4. The vertical lines mark the times when the SEDs of the afterglow were determined as shown in Fig. 10.

rest-frame $\beta_{oX}$ of $0.85 \pm 0.10$ at 800 s, $0.84 \pm 0.05$ at 20 ks, $0.74 \pm 0.07$ at 100 ks, and $0.77 \pm 0.10$ at 500 ks after the burst. Within the errors these values are consistent and do not suggest any changes between the optical/UV and X-ray parts of the SED over time after the first orbit. However, note that during the first $\approx$400 s of data the SED changes dramatically, because the X-ray flux decays very fast ($\alpha_{X,1} = 5.1$, while the white and $V$ data suggest that the optical afterglow is constant. A single–power-law spectrum between optical/UV and X-ray energies a $\beta_{oX} = 1.1$ is expected according to the fits to the X-ray data (Table 3). This assumption of a single–power-law spectrum between the optical and X-rays is justified given that the optical has the same temporal behavior as the X-rays and the optical and X-rays are both above the cooling frequency. The difference between the expected $\beta_{oX} = 1.1$ and the measured $\beta_{oX} \approx 0.8$ values suggests intrinsic reddening at the location of the afterglow. Based on the absorption corrected rest-frame 2 keV flux density, we can calculate the expected flux density at rest-frame 2500 Å. We calculated a

TABLE 5
Decay Slopes and Break Times of the UVOT Light Curves

| Filter | $\alpha_2$[a] | $T_{break}$[b] | $\alpha_3$ |
|---|---|---|---|
| $V$ | $0.24 \pm 0.05$ | $40^{+15}_{-15}$ | $1.21 \pm 0.09$ |
| $B$ | $0.16 \pm 0.05$ | $30^{+20}_{-10}$ | $0.96 \pm 0.05$[c] |
| $U$ | $0.41 \pm 0.07$ | $54^{+10}_{-15}$ | $1.40 \pm 0.07$ |
| UVW1 | $0.47 \pm 0.06$ | $48^{+5}_{-5}$ | $1.29 \pm 0.03$ |
| UVM2 | $0.35 \pm 0.10$ | $50^{+5}_{-15}$ | $1.39 \pm 0.05$ |
| UVW2 | $0.46 \pm 0.07$ | $55^{+5}_{-10}$ | $1.36 \pm 0.04$ |
| X-rays | $0.14 \pm 0.02$ | $57^{+10}_{-10}$ | $1.29 \pm 0.03$ |

Note.—The decay slopes $\alpha_2$ and $\alpha_3$ follow the conventions in Zhang et al. (2006) and Nousek et al. (2006).

[a] Decay slope before the energy injection and rebrightening at 20 ks after the burst.

[b] Time after the break in ks in the observed frame.

[c] Note that when limiting the analysis of the late time decay slope $\alpha_3$ to 50–200 ks after the burst, the decay slope is $1.17 \pm 0.16$.

reddening of 1.7 mag at rest-frame 2500 Å, which corresponds to an $E_{B-V} = 0.34$ mag. Applying the relation given by Diplas & Savage (1994),[15] we calculated an intrinsic column density $N_{H,intr} = 1.7 \times 10^{21}$ cm$^{-2}$. Considering that this is a rough estimate, this absorption column density agrees quite well with that measured from the *XMM-Newton* EPIC pn spectrum, $N_{H,intr} = 0.85 \pm 0.02 \times 10^{21}$ cm$^{-2}$ (Table 3).

## 4. DISCUSSION

The afterglow of GRB 060729 has been detected in X-rays by the *Swift* XRT longer than any other *Swift*-detected burst, up to 125 days after the burst. Finally, by the end of 2006 December, we had to give up on observing this burst by *Swift* because it became too faint to be detectable in the XRT detector. Even though the afterglow was dropped from the *Swift* observing schedule after 2006 December 27, we are still planning to obtain more observations with larger observatories, such as *Chandra*, *XMM-Newton*, and *Suzaku*.

[15] The Diplas & Savage (1994) relation is $N_H = 4.93 \times 10^{21} \times E_{B-V}$ cm$^{-2}$.

### 4.1. *Light Curves*

The X-ray and UV/Optical light curves are remarkably similar. Not only are their decay slopes and break times are in good agreement (except for the *B* light curve), but they also seem to be synchronized during rebrightening phases, which can be seen best in the UVW2 light curve. In particular, the rebrightening at about 15 ks after the burst clearly appears to be present in all six UVOT filters and in X-rays. Even though the break at around 50 ks after the burst seems to be achromatic, we do not consider this to be a jet break. The postbreak decay slope $\alpha_{X,3} = 1.29$ is to shallow to be a jet break. If we interpret this slope as the post jet break slope, we would get $p = 1.29$, which is much flatter than the electron distribution index predicted by shock acceleration theory (usually $p \gtrsim 2$). Furthermore, if $p = 1.29$, one would expect the spectral slope $\beta_X = p/2 = 0.65$ or $\beta_X = (p-1)/2 = 0.15$ for a cooling frequency below or above the X-ray range, respectively, which is obviously contrary to the observed spectral slope of $\beta_X = 1.1$ Most likely we have not seen the jet break in the afterglow of GRB 060729 because the afterglow has not been followed long enough, as the studies by Willingale et al. (2007) and Sato et al. (2007) suggest.

One of our main results is that the light curve of the afterglow does not yet show a jet break at 125 days after the burst (81 days in the rest frame). This is the longest period a GRB afterglow was ever followed and detected in X-rays, except for GRB 030329, which was followed 258 days after the burst by *XMM-Newton* (Tiengo et al. 2004). According to the relation given in Willingale et al. (2007) we would have expected to see a jet break at about $5.5 \times 10^6$ s after the burst. With an isotropic energy in the rest-frame 1 keV–10 MeV of $E_{iso} = 1.6 \times 10^{52}$ ergs and the relations given by Sari et al. (1999) and Frail et al. (2001), as well as the nondetection of a jet break up to 125 days after the burst, we

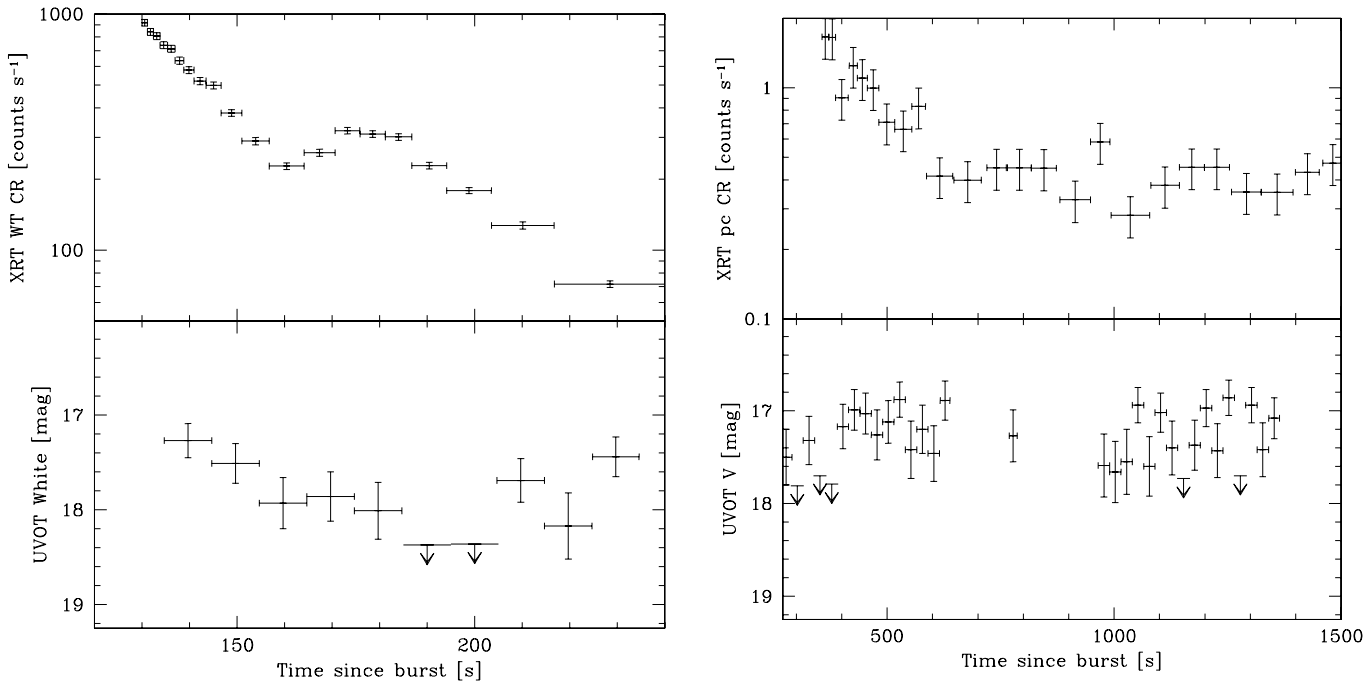


Fig. 9.—*Swift* UVOT white and *V* and XRT WT PC-mode early-time light curves of the first orbit. The left panel shows the UVOT white and the XRT WT mode data, and the right panel shows UVOT *V* and XRT PC-mode data. The binning in the PC-mode data is 25 photons bin$^{-1}$. The UVOT white data are binned in 10 s intervals and the *V* data are binned in 25 s intervals.

TABLE 6

List of the *Swift* UVOT White and *V* Observations during the First Orbit as Shown in Figure 9

| Time[a] | White | *V* |
|---|---|---|
| 140 | 17.27 ± 0.18 | ... |
| 150 | 17.51 ± 0.21 | ... |
| 160 | 17.93 ± 0.27 | ... |
| 170 | 17.86 ± 0.26 | ... |
| 180 | 18.01 ± 0.30 | ... |
| 190 | 3σul: 18.37 | ... |
| 200 | 3σul: 18.36 | ... |
| 210 | 17.69 ± 0.23 | ... |
| 220 | 18.17 ± 0.35 | ... |
| 230 | 17.44 ± 0.21 | ... |
| 278 | ... | 17.50 ± 0.30 |
| 303 | ... | 3σul: 17.81 |
| 328 | ... | 17.32 ± 0.26 |
| 353 | ... | 3σul: 17.70 |
| 378 | ... | 3σul: 17.79 |
| 403 | ... | 17.17 ± 0.24 |
| 428 | ... | 16.99 ± 0.22 |
| 453 | ... | 17.03 ± 0.22 |
| 478 | ... | 17.26 ± 0.27 |
| 503 | ... | 17.12 ± 0.23 |
| 528 | ... | 16.88 ± 0.19 |
| 553 | ... | 17.42 ± 0.31 |
| 578 | ... | 17.20 ± 0.26 |
| 603 | ... | 17.46 ± 0.30 |
| 628 | ... | 16.89 ± 0.21 |
| 778 | ... | 17.27 ± 0.28 |
| 978 | ... | 17.59 ± 0.34 |
| 1003 | ... | 17.66 ± 0.33 |
| 1028 | ... | 17.55 ± 0.35 |
| 1053 | ... | 16.94 ± 0.19 |
| 1078 | ... | 17.60 ± 0.32 |
| 1103 | ... | 17.02 ± 0.21 |
| 1128 | ... | 17.40 ± 0.29 |
| 1153 | ... | 3σul: 17.73 |
| 1178 | ... | 17.37 ± 0.27 |
| 1203 | ... | 16.97 ± 0.20 |
| 1228 | ... | 17.43 ± 0.29 |
| 1253 | ... | 16.86 ± 0.19 |
| 1278 | ... | 3σul: 17.70 |
| 1303 | ... | 16.94 ± 0.19 |
| 1328 | ... | 17.42 ± 0.29 |
| 1353 | ... | 17.08 ± 0.22 |
| 1503 | ... | 3σul: 17.19 |
| 1528 | ... | 3σul: 17.81 |
| 1678 | ... | 16.96 ± 0.27 |

[a] The times note the middle of the observation in s after the burst.

TABLE 7

List of the *XMM-Newton* Optical Monitor Observations

| ObsID | $T_{obs}$[a] (s) | Filter | Mag |
|---|---|---|---|
| 006 | 48,351 | *U* | 17.27 ± 0.02 |
| 018 | 52,707 | *U* | 17.43 ± 0.02 |
| 010 | 70,984 | UVW1 | 17.53 ± 0.04 |
| 015 | 75,291 | UVW1 | 17.57 ± 0.04 |
| 016 | 84,105 | UVW1 | 17.71 ± 0.04 |
| 020 | 88,612 | UVW1 | 17.83 ± 0.05 |
| 012 | 92,919 | UVM2 | 17.89 ± 0.12 |
| 014 | 97,226 | UVM2 | 17.98 ± 0.13 |
| 017 | 101,533 | UVM2 | 17.73 ± 0.11 |

[a] The times note the middle of the observation in seconds after the burst.

derive that the opening angle of the jet to be larger than 28°, assuming a particle density $n = 0.1$ cm$^{-3}$ and an efficiency $\eta_\gamma = 0.2$. With $\beta_X = 1.0$ and $\alpha_X = 1.29$, according to Table 2 in Zhang et al. (2006), we estimated an electron index slope $p = 2.3$ for the ISM or wind case with $\nu > \max(\nu_m,\ \nu_c)$.

The afterglow of GRB 060729 is not only remarkable for its long follow-up observations in X-rays but also for its relatively late break time between the flat decay phase and the steepening phase (phases 2 and 3, according to Zhang et al. 2006; Nousek et al. 2006; Willingale et al. 2007) at about 53 ks after the burst, which converts to 35 ks in the rest frame. Typically, the break between phases 2 and 3 occurs around 10 ks after the burst (Nousek et al. 2006; Willingale et al. 2007). The late-time break at 35 ks after the burst (rest frame) requires a substantial ongoing injection of energy into the afterglow. As a matter of fact, when we observed this afterglow with *Swift* we did not detect a break in the light curve until about 2 days after the burst due to the lumpiness of this plateau phase. Also note that Willingale et al. (2007) list the break time in the X-ray light curve at 120 ks after the burst.

The relatively long period of this very flat decay ($\alpha_{X,2} = 0.14 \pm 0.02$) phase implies larger energy injection during the early time in this burst than in other bursts. This energy injection could be the result of a refreshed shock (Rees & Mészáros 1998) or of continuous energy input from the central engine. Assume the energy injection has the form $L(t) \propto t^{-q}$, the light-curve decay rate is $[(2p - 4) + (p + 2)]q/4$ for $\nu_X > \max(\nu_m,\ \nu_c)$ (Zhang et al. 2006). So we get $q \simeq 0$, and the total energy is increased by a factor of $(T_{break,2}/T_{break,1})^{1-q} \sim 100$ during this energy injection phase, where $T_{break,1}$ and $T_{break,2}$ are the first and second break time of the X-ray light curve, respectively. Such a large energy increase factor is the highest among the *Swift*-detected GRBs (Nousek et al. 2006). This may be part of the reason that we see a bright X-ray afterglow for a very long time, aside from the fact that no jet break occurs before 125 days after the burst. The plateau phase of the X-ray afterglow of GRB 060729 is one of the longest ever observed by *Swift*. The total fluence in the 0.3–10.0 keV band of this plateau is about $1 \times 10^{-6}$ ergs cm$^{-2}$, which is about $\frac{1}{3}$ of the total 15–150 keV fluence of the prompt emission. The $q$-value ($q = 0$) inferred for this burst implies a pulsar type (i.e., magnetic dipole radiation) energy injection (e.g., Dai & Lu 1998; Zhang & Mészáros 2001).

Using the X-ray luminosity $L_X = 2 \times 10^{46}$ ergs s$^{-1}$ at $t = 10\ h$, we estimate the isotropic kinetic energy at this time is $E_{k,iso} \sim 2.5 \times 10^{53}(\epsilon_e/0.1)^{-1}$ ergs (Freedman & Waxman 2001; Zhang et al. 2007a), where $\epsilon_e$ is the equipartition factor of electrons in afterglow shocks. Assuming that the energy increases by a factor 100 during the flat decay phase, the isotropic kinetic energy before the energy injection phase is only $\sim 2.5 \times 10^{51}(\epsilon_e/0.1)^{-1}$ ergs, implying highly efficient gamma-ray production during the prompt phase. Using the isotropic kinetic energy and the jet break time greater than 125 days after the burst, we get the jet opening angle larger than $\theta_j \gtrsim 28° n_{-1}^{1/8}$ (Frail et al. 2001), where $n_{-1} \equiv (n/0.1\ \text{cm}^{-3})$ is the number density of the circumburst ISM. From this we further get the beam-corrected kinetic energy of the burst $E_{k,j} \gtrsim 1.7 \times 10^{52}$ ergs $(\epsilon_e/0.1)^{-1} n_{-1}^{1/4}$. This kinetic energy is greater than that seen in usual bursts and may be a direct consequence of the unusually long energy injection phase in the early time.

Even though the X-ray and UV/optical afterglow of GRB 060729 was unusually bright, it was rather unspectacular in the BAT 15–150 keV energy range. The 15–150 keV fluence of $2.7 \times 10^{-6}$ ergs cm$^{-2}$ (Parsons et al. 2006) is rather moderate compared to other *Swift*-discovered bursts. Also note that the peak

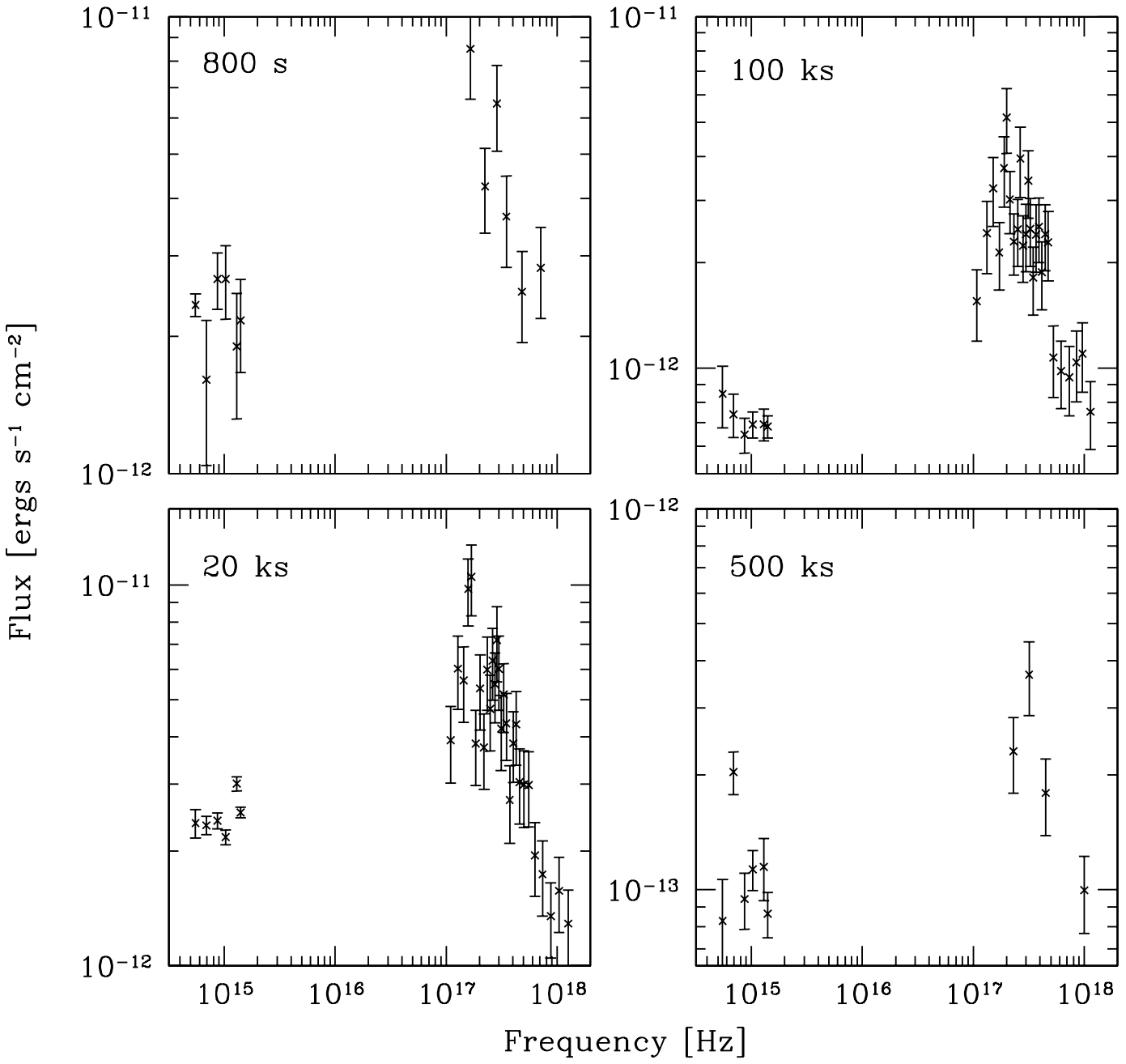


FIG. 10.— SEDs of the afterglow of GRB 060729 at 800 s (*top left*), 20 ks (*bottom left*), 100 ks (*top right*), and 500 ks (*bottom right*). The UVOT photometry data are corrected for Galactic reddening ($E_{B-V} = 0.050$; Schlegel et al. 1998).

luminosity of GRB 060729 of about $3 \times 10^{50}$ ergs s$^{-1}$ is very low for a long burst considering the time lag between the 50–100 and 15–25 keV band, as shown by Gehrels et al. (2006).

The observations of the X-ray and UV fields of GRB 060729 have been the deepest ever performed by *Swift*. In X-rays we observed the field for 1.13 Ms and for 550 ks each in UVW1 and UVW2. The UVW1 and UVW2 observations are the longest exposure taken of any field in the UV by any UV observatory. The results of this study and the source identifications based on the resulting SEDs will be presented in a separate paper, which is in preparation.

### 4.2. *Spectra Analysis of the Early-Time Data*

During the XRT WT mode epoch of observations, two flares are detected. For the first X-ray flare, only the decay part is seen by the XRT. The decay rates after the peak of the flares are as steep as $t^{-5}$, pointing to internal central engine activity as the origin for the X-ray flares (Burrows et al. 2005b; Fan & Wei 2005; Zhang et al. 2006; Dai et al. 2006; Falcone et al. 2006; Wu et al. 2006; Wang et al. 2006; Lazzati & Perna 2007; Gao & Fan 2006).

During 130–160 s (time bins from 1 to 11 in Table 2) and 190–300 s, the X-ray emission is undergoing a steep decay, which may result from the high-latitude emission of the corresponding flares (Kumar & Panaitescu 2000; Liang et al. 2006); i.e., we see the curvature effect of the radiation pulse. In this picture the count rate and the peak energy ($kT$ or $E_{\rm break}$) both decrease as the pulse decays. This is because less and less Doppler-boosted radiation is seen from the pulse. This accounts for the strong correlation between the count rate and the blackbody temperature $kT$ (Spearman rank order correlation coefficient $R_{\rm S} = 0.96$ with $T_{\rm S} = 11.8$ and

a probability of $P < 10^{-4}$ of a random distribution; linear correlation coefficient $r_l = 0.95$).

The WT data of the early afterglow observations showed a dramatic change in the X-ray spectrum within less than 2 minutes in the rest frame. Typically, the spectra of the bins of the WT mode data can be fitted by a single–absorbed-power-law or a blackbody plus power-law model. The power-law model shows that there is a decrease in the absorption column density by a factor of 4 from the beginning of the observation at 131 s after the burst to 300 s after the burst. Such decreases in the absorption column density have been observed before in GRB afterglows (e.g., in GRB 050712; De Pasquale et al. 2006; Lazzati & Perna 2002) but have been usually linked to a flattening of the X-ray spectral slope. This is typically an artifact of the spectral fitting routine, which may be due to the correlation between spectral parameters such as $N_{\rm H}$ and $\beta_{\rm X}$. However, the situation in GRB 060729 is completely different. Here we observe not only a decreasing absorption column density $N_{\rm H}$, but also a steepening of the X-ray spectral slope $\beta_{\rm X}$, which is the opposite of what one expects if this is just an artifact of the fitting routine. Therefore, we consider the decrease of the absorption column density to be real. There are two explanations for a decrease in the column density of a neutral absorber: (1) an expanding medium that results in a lower volume and column density and (2) ionization of the neutral gas. Both of these, the expansion and the ionization of the gas, happen after the explosion of the star. A softening of the X-ray spectrum during the initial decline has been commonly observed as reported by Zhang et al. (2007b).

Alternatively the WT mode spectra can also be fitted with a blackbody plus power-law model. In order to limit the number of free parameters, the absorption column density parameter was set to the Galactic value. These fits show a decrease of the blackbody temperature from about 0.6 keV to about 0.1 keV from the beginning to the end of the WT observing period. Fixing the absorption column density to a value of $1 \times 10^{21}$ cm$^{-2}$, the value obtained at later times during the *XMM* observation, results in similar values for the blackbody temperature. From these fits the temperature tends to be slightly lower than when fixing the $N_{\rm H}$ to the Galactic value. However, within the errors the results are consistent. The biggest influence the increase in the absorption column density has is on the normalization of the blackbody and power-law components.

In the latter scenario the thermal component is likely to be the photospheric emission from X-ray flares. In the prompt GRB phase we have seen the thermal emission from some bursts (e.g., Ryde et al. 2006), which has been interpreted as the photospheric emission when the fireball becomes optically thin (Mészáros & Rees 2000; Rees & Mészáros 2005; Thompson et al. 2007; Ramirez-Ruiz 2005; Pe'er et al. 2006). Since X-ray flares are believed to be the result of late-time central engine activity with a radiation mechanism similar to the prompt phase, a photosphere component found in X-ray flares is reasonable. The thermal emission component discovered from GRB 060729 also supports the internal origin of the X-ray flares, rather than external shocks. Let us examine the relation between the blackbody radius $R_{\rm bb}$ derived from the spectral fitting and the photosphere radius $R_{\rm ph}$. For a relativistic moving source, the luminosity of the thermal component at the photospheric radius is

$$L = 4\pi R_{\rm ph}^2 \Gamma^2 \sigma T'^4, \quad (1)$$

where $T'$ is the photospheric temperature in the comoving frame and $\Gamma$ is the bulk Lorentz factor. As the usual fitting uses $L = 4\pi R_{\rm bb}^2 \sigma T^4$, we get $R_{\rm ph} = \Gamma R_{\rm bb}$ by taking advantage of $T = \Gamma T'$. The fitted blackbody radii around the peak of the X-ray flares are a few times $10^{12}$ cm. This means the photospheric radii of the two X-ray flares in GRB 060729 are a few times of $10^{12}$ $\Gamma$ cm. The photospheric radius is very sensitive to the bulk Lorentz factor $\Gamma$ of the fireball (Rees & Mészáros 2005) and a photospheric radius of $10^{13}$–$10^{14}$ cm is reasonable if $\Gamma$ of the X-ray flare is of the order of 10.

During the early steep decay phase, the bolometric flux (equivalent to the flux in XRT band if the peak energy located within the 0.3–10 keV range of the XRT) may decrease as $F_{\rm X}(t) \propto (t - t_0)^{-2}$ due to the curvature effect (Ryde & Petrosian 2002), where $t_0$ is some reference time of the flare (Liang et al. 2006) and the peak energy decays as $(t - t_0)^{-1}$. So, if we fit the spectrum with the blackbody model [$F_{\rm X}(t) \propto T^4 R_{\rm bb}^2$] all the time during the decay phase, we would expect that the blackbody radius increases with time as $R_{\rm bb} \propto (t - t_0)$. This may explain the apparent increase of the blackbody radius with time during the steep phase of the flares.

## 5. CONCLUSIONS AND SUMMARY

We studied the *Swift* and *XMM-Newton* observations of the afterglow of GRB 060729 and found:

1. The light curve of the afterglow extends out to 125 days after the burst (81 days in the rest frame) without showing any sign of a jet break. We estimated that the jet opening angle has to be larger than 28°. This is the longest follow-up and detection of a GRB afterglow in X-rays ever performed, except for GRB 030329.
2. The X-ray light curve can be generally described by an initial steep decay slope $\alpha_1 = 5.1 \pm 0.2$, a break time $T_{\rm break,1} = 530 \pm 25$ s, flat decay slope $\alpha_2 = 0.14 \pm 0.02$ with a break at $T_{\rm break,2} = 56.8 \pm 10$ ks, and a steep decay slope $\alpha_3 = 1.29 \pm 0.03$.
3. The unusually long flat decay phase of the afterglow of GRB 060729 implies a much larger energy injection than seen in any other GRB afterglow.
4. After the initial phase, the light curves in X-rays as well as in all six UVOT filters follow the same shape.
5. In the initial phase the afterglow shows a dramatic change in its X-ray spectrum, which can either be described by a steepening of a power-law spectrum with a simultaneous decrease in the intrinsic column density or by a decrease in the blackbody temperature from 0.6 keV at 130 s after the burst to 0.1 keV at 250 s observed after the burst.
6. The spectral analysis of the *Swift* XRT PC mode and *XMM-Newton* EPIC pn and MOS data shows that the X-ray spectrum of the afterglow agrees with an absorbed power law with $\beta_{\rm X} = 1.1$ and an intrinsic column density $N_{\rm H,intr} = 1 \times 10^{21}$ cm$^{-2}$.
7. The reddening and intrinsic column density estimated from the spectral energy distribution agrees well with the value found from the *XMM-Newton* analysis.

We would like to thank Dmitry Frederiks for checking the Konus-*Wind* measurements of the time of the burst and the anonymous referee for a constructive and detailed referee's report that significantly improved the paper. This research has made use of data obtained through the High Energy Astrophysics Science Archive Research Center Online Service, provided by the NASA/Goddard Space Flight Center. This research was supported by NASA contract NAS5-00136 and SAO grant G05-6076X BASIC.

REFERENCES


Abbey, T. 2006, The X-ray Universe, ed. A. Wilson (ESA-SP 604; Noordwijk: ESA), 943
Arnaud, K. A. 1996, ASP Conf. Ser. 101, Astronomical Data Analysis Software and Systems V, G. H. Jacoby & J. Barnes (San Francisco: ASP), 17
Band, D., et al. 1993, ApJ, 413, 281
Barthelmy, S. D., et al. 2005, Space Sci. Rev., 120, 143
Blustin, A. J., et al. 2006, ApJ, 637, 901
Burrows, D. N., et al. 2005a, Space Sci. Rev., 120, 165
———. 2005b, Science, 309, 1833
———. 2006, ApJ, 653, 468
Campana, S., & De Luca, A. 2006, GCN Circ. 5469, http://gcn.gsfc.nasa.gov/gcn3/5469.gcn3
Campana, S., et al. 2006, Nature, 442, 1008
Cobb, B. E., & Bailyn, C. D. 2006, GCN Circ. 5465, http://gcn.gsfc.nasa.gov/gcn3/5465.gcn3
den Herder, J. W., et al. 2001, A&A, 365, L7
Dai, Z. G., & Lu, T. 1998, A&A, 333, L87
Dai, Z. G., Wang, X. Y., Wu, X. F., & Zhang, B. 2006, Science, 311, 1127
De Pasquale, M., et al. 2006, MNRAS, 370, 1859
Dickey, J. M., & Lockman, F. J. 1990, ARA&A, 28, 215
Diplas, A., & Savage, B. D. 1994, ApJ, 427, 274
Fan, Y. Z., & Wei, D. M. 2005, MNRAS, 364, L42
Falcone, A., et al. 2006, ApJ, 641, 1010
Frail, D. A., et al. 2001, ApJ, 562, L55
Freedman, D. L., & Waxman, E. 2001, ApJ, 547, 922
Gao, W.-H., & Fan, Y.-Z. 2006, Chinese J. Astron. Astrophys., 6, 513
Gehrels, N., et al. 2004, ApJ, 611, 1005
———. 2006, Nature, 444, 1044
Grupe, D. 2006, GCN Circ. 5369, http://gcn.gsfc.nasa.gov/gcn3/5369.gcn3
Grupe, D., et al. 2006, GCN Circ. 5365, http://gcn.gsfc.nasa.gov/gcn3/5365.gcn3
Haberl, F., Schwope, A. D., Hambaryan, V., Hasinger, G., & Motch, C. 2003, A&A, 403, L19
Hill, J. E., et al. 2004, Proc. SPIE, 5165, 217
Hogg, D. 1999, preprint (astro-ph/9905116)
Immler, S. 2006, GCN Circ. 5367, http://gcn.gsfc.nasa.gov/gcn3/5367.gcn3
Jansen, F., et al. 2001, A&A, 365, L1
Kumar, P., & Panaitescu, A, 2000, ApJ, 541, L51
Lazzati, D., & Perna, R. 2002, MNRAS, 330, 383
———. 2007, MNRAS, 375, L46
Liang, E., et al. 2006, ApJ, 646, 351
Mangano, V., et al. 2007, A&A, in press
Mason, K. O., et al. 2001, A&A, 365, L36
Mészáros , P., & Rees, M. J. 2000, ApJ, 530, 292
Nousek, J., et al. 2006, ApJ, 642, 389
O'Brien, P. T., et al. 2006, ApJ, 647, 1213
Pagani, C., et al. 2006, ApJ, 645, 1315
Page, K. L., et al. 2007, ApJ, in press
Parsons, A., et al. 2006, GCN Circ. 5370, http://gcn.gsfc.nasa.gov/gcn3/5370.gcn3
Pe'er, A., Mészáros , P., & Rees, M. J. 2006, ApJ, 652, 482
Quimby, R., & Rykoff, E. S. 2006, GCN Circ. 5377, http://gcn.gsfc.nasa.gov/gcn3/5377.gcn3
Quimby, R., Swan, H., Rujopakarn, W., & Smith, D. A. 2006, GCN Circ. 5366, http://gcn.gsfc.nasa.gov/gcn3/5366.gcn3
Ramirez-Ruiz, E. 2005, MNRAS, 363, L61
Rees, M. J., & Mészáros, P. 1998, ApJ, 496, L1
———. 2005, ApJ, 628, 847
Romano, P., et al. 2006, A&A, 456, 917
Roming, P. W. A., et al. 2005, Space Sci. Rev., 120, 95
Ryde, F., Björnsson, C.-I., Kaneko, Y., Mészáros , P., Preece, R., & Battelino, M. 2006, ApJ, 652, 1400
Ryde, F., & Petrosian, V. 2002, ApJ, 578, 290
Sari, R., Piran, T., & Halpern, J. P. 1999, ApJ, 519, L17
Sato, G., et al. 2007, ApJ, 657, 359
Schartel, N. 2006, GCN Circ. 5368, http://gcn.gsfc.nasa.gov/gcn3/5368.gcn3
Schlegel, D. J., Finkbeiner, D. P., & Davis, M. 1998, ApJ, 500, 525
Strüder, L., et al. 2001, A&A, 375, L5
Tananbaum, H., et al. 1979, ApJ, 234, L9
Thoene, C. C., et al. 2006, GCN Circ. 5373, http://gcn.gsfc.nasa.gov/gcn3/5373.gcn3
Thompson, C., Mészáros , P., & Rees, M. J. 2007, ApJ, submitted, astro-ph/0608282
Tiengo, A., Mereghetti, S., Ghisellini, G., Tavecchio, F., & Ghirlanda, G. 2004, A&A, 423, 861
Turner, M. J. L., et al. 2001, A&A, 365, L27
Vaughan, S., et al. 2006, ApJ, 638, 920
Wang, X. Y., Li, Z., & Mészáros , P. 2006, ApJ, 641, L89
Willingale, R., et al. 2007, ApJ, submitted (astro-ph/0612031)
Wu, X. F., et al. 2006, ApJ, astro-ph/0512555
Zhang, B., Fan, Y. Z., Dyks, J., Kobayashi, S., Mészáros, P., Burrows, B. N., Nousek, J. A., & Gehrels, N. 2006, ApJ, 642, 354
Zhang, B., & Mészáros, P. 2001, ApJ, 552, L35
Zhang, B., et al. 2007a, ApJ, 655, 989
Zhang, B.-B., Liang, E. W., & Zhang, B. 2007b, ApJ, submitted (astro-ph/0612246)